Remote Sensing of Environment 255 (2021) 112272

Contents lists available at ScienceDirect

Remote Sensing of Environment

journal homepage: www.elsevier.com/locate/rse

SPLITSnow: A spectral light transport model for snow

Petri M. Varsa *, Gladimir V.G. Baranoski, Bradley W. Kimmel

NPSG, D.R. Cheriton School of Computer Science, University of Waterloo, Waterloo, Ontario N2L 3G1, Canada

ARTICLE INFO

Keywords:
Snow
Radiative transfer model
Scattering
Ray tracing
BSSRDF
BSDF
Reflectance
Transmittance

ABSTRACT

Snow is a fundamental component of the climate system. It is also an important part of the planet's hydrological cycle. Accordingly, the investigation of its light scattering properties is essential for remote sensing applications employed in the estimation of changes in the current amount of snowpack. These wide-scale environmental changes are key indicators of future climate events affecting global sustainability. Viewed in this context, computational simulations of light interactions with snow can be used to increase the effectiveness-to-cost ratio of remote sensing initiatives in this area. More specifically, by enabling a controlled assessment of the effects of snow granular structure and composition parameters on its light reflection and transmission profiles, these simulations can be instrumental in the high-fidelity interpretation of data remotely acquired from snow-covered landscapes that pose sizable challenges for field work. In order to contribute to these interdisciplinary research efforts, this paper presents a novel light transport model for snow that can predictively simulate the spectral and spatial distributions of light interacting with this ubiquitous particulate material. While the former radiometric responses are quantified in terms of hyperspectral reflectance and transmittance, the latter are quantified in terms of BSDF (bidirectional scattering distribution function). The proposed model employs a first-principles simulation approach that accounts for the positional dependence of the scattered light in the quantification of its spatial distribution. Thus, this distribution can also be expressed in terms of BSSDF (bidirectional surface-scattering distribution function). The predictive capabilities of the proposed model are quantitatively and qualitatively evaluated by comparing modeled results with measured data obtained from *in situ* experiments and phenomenological traits reported in the literature, respectively.

1. Introduction

Snow is a granular material composed of ice crystals. Grains are typically millimeter or submillimeter in size. The grains can be smooth and round, faceted and crystalline, or may possess dendritic (branching) features (Fierz et al., 2009). The volume fraction of space between the grains is known as the *pore space*. This space is composed of air, and often to a lesser extent, water.

The study of light transport through snow grains is a complex problem with numerous applications in remote sensing. The high reflectance and insular properties of snow make it a fundamental component of the climate system for the cryosphere (Barry, 1985). Snow is also an important part of the hydrological cycle delivering potable water in snowmelt-dominated regions. Global surface temperature changes alter the seasonality of meltwater run off, thus affecting the temporal availability of fresh water (Barnett et al., 2005; Metsämäki et al., 2018; Han et al., 2019). In addition to environmental factors, modeling the electromagnetic radiation interactions with snow has pragmatic applications such as determining snow's effect on sensitive equipment (Wang et al., 2005). Accurate measurements of snow reflectance are required in order to gain valuable insights into these areas, and these measurements are subject to various properties of snow. *In situ* measurements of snow are costly and not without issues (Kinar and Pomeroy, 2015). Furthermore, inhospitable regions also need regular seasonal measurement *via* remote sensing techniques. A detailed knowledge of how light interacts with snow grains is essential to facilitate accurate interpretation of the resulting remote sensing data. The effects of the various features of deposited snow on its spectral reflectance can be appropriately studied using an *in silico* (computer simulation) investigation approach. The application of this approach in the analysis of the interaction between electromagnetic radiation and water-ice grains can accelerate the understanding of the causal attributes of snow reflectance since each parameter can be varied individually. By comparison, *in situ* field experiments are subject to multiple

* Corresponding author.
E-mail address: pmvarsa@uwaterloo.ca (P.M. Varsa).

https://doi.org/10.1016/j.rse.2020.112272
Received 7 May 2020; Received in revised form 20 November 2020; Accepted 18 December 2020
Available online 12 January 2021

simultaneous parameter changes due to environmental factors. Similarly, manufacturing artificial snow grains is time consuming and costly, and precise traits are still subject to temporal metamorphism (Colbeck, 1982, 1997). *In silico* simulations can also be employed to provide a complementary data source for testing analytic models by providing data with good angular sampling that may not otherwise be readily available (Ding et al., 2019).

To date, a number of geophysical works on the modeling of light interactions with snow have focused on simulating single scattering events elicited by individual grains. This is then used as an input to a larger analytic theory (Bohren and Barkstrom, 1974; Bohren, 1983; Yang and Liou, 1996; Grundy et al., 2000; Jin et al., 2008). Others have used tomographic scans of snow either as the basis of, or as inspiration for, a multiple scattering model (Kaempfer et al., 2007; Bänninger et al., 2008; Haussener et al., 2012; Xiong and Shi, 2014, 2017, 2018; Xiong et al., 2015). Finally, other works have employed a ray tracing technique based on geometrical (ray) optics (Born and Wolf, 1999), henceforth referred to simply as *ray tracing*, to investigate multiple scattering by simulating photon paths through a large collection of objects that are meant to represent snow grains. These shapes include hemispherically-capped cylinders (Kaempfer et al., 2007), cubes, hexahedra, cylinders, hyperboloids and combinations thereof (Picard et al., 2009). Multiple scattering models are more complex. However, they are able to capture angular effects of reflection (Dozier and Painter, 2004). Current multiple scattering approaches that model individual grains are limited by the vast quantity of grains that must be stored, sorted and retrieved. Whereas models that employ data acquired from a tomographic scan (Kaempfer et al., 2007) are limited to the study of the specific sample.

Geometric optics have been successfully employed for the study of particulate materials other than snow such as sand-textured soils (Kimmel and Baranoski, 2007). It has been noted that there are similarities between granular materials, such as soil and snow, when considering scales sufficiently larger than the wavelength of light (Mishchenko et al., 1999; Bänninger and Flühler, 2004). Indeed, knowledge of the mineralogical similarities between ice crystals and other minerals dates back to the twelfth century (Needham and Lu, 1961).

In this work, we present a novel light transport model for snow, henceforth referred to as SPLITSnow (*SP*ectral *LI*ght *T*ransport in *S*now). It builds upon a proven first-principles approach previously used to the simulate light interactions with sand-textured soils (Kimmel and Baranoski, 2007). This approach accounts for a wide variety of physical phenomena exhibited by granular materials *via* the stochastic generation of grains on the fly throughout the simulation process. While other multiple scattering models that employ ray tracing geometric optics are constrained by the computer memory and the computational complexity of managing a large dataset of grains, this stochastic approach makes use of a single grain at a time. Thus, even semi-infinite samples are within reasonable computational limits without requiring expensive hardware resources. Furthermore, the stochastic generation of surface properties allows for detailed modeling of complex geometries without the requirement to store these primitive shapes. The proposed model can predictively simulate the spectral and spatial distributions of light interactions with snow. The spectral radiometric responses are quantified in terms of hyperspectral reflectance and transmittance, whereas the spatial radiometric responses are quantified in terms of scattering distribution functions.

The BSSRDF (bidirectional surface-scattering reflectance-distribution function) encapsulates the geometric reflectance properties of a material Nicodemus et al. (1977). A first-principles approach, such as the one employed in the proposed framework, is capable of capturing these geometric reflectance outputs. However, for many applications, the exit location parameters are not employed. For these circumstances where the scattering function does not depend upon the location of exitance, and the area of irradiance is relatively large, then only the directional components can be considered, yielding the BSDF (Bartell et al., 1981). If only the reflected portion of the BSDF is of concern, it can be expressed in terms of the BRDF (bidirectional reflectance distribution function). Similarly for the transmitted portion, it can be expressed in terms of the BTDF (bidirectional transmittance distribution function).

Snow reflectance is known to be affected by morphological changes within the accumulated snowfall (Lyapustin et al., 2009). As snow ages, a decrease in overall reflectance can be observed, in part due to an overall increase in grain size (Wiscombe and Warren, 1980; Barry, 1985). In addition to grain size, there are several other parameters that may have an impact.

Grain size is the most studied parameter, as it is known to be a significant contributor to reflectance. As the grain size increases, absorption increases and reflectance decreases. Thus, the effect grain size has on transmittance is complex. Kokhanovsky et al. (2020) observed that transmittance may either increase or decrease, depending upon the wavelength. For the snow grain sizes and wavelengths considered in this work, an increase in grain size will decrease reflectance (Nakamura et al., 2001) and increase transmittance (Bänninger and Flühler, 2004; Ciani et al., 2005). In particular, sensitivity to grain size in the near infrared (700–1300 nm) has been used in remote sensing applications (Nolin and Dozier, 1993, 2000) to estimate the effective grain size (Grenfell and Warren, 1999) of the accumulated snowfall, commonly referred to as the snowpack. However, other factors also contribute to reflectance. For example, a significant amount of light is absorbed by water in the near infrared domain (Hale and Querry, 1973), which reduces the amount of reflected light (Green et al., 2002). Even dry snow is active thermodynamically, which induces morphological changes on the snow grains (Colbeck, 1982, 1997).

Reliable approximations to spectral reflectance (Nicodemus et al., 1977) can be obtained by models that represent grains as spheres and only account for grain size. However, when the angular dependence of reflectance is investigated, then more complex grain shapes should be incorporated (Dozier and Painter, 2004; Kokhanovsky and Zege, 2004). In particular, precipitating snow is known to have more crystalline features. Over a period of days, vapor pressure gradients within the snow erode the facets, and the grains become a rounded prolate spheroid (Colbeck, 1982). Thus, the age of the snow affects the directional reflectance.

The remainder of this paper is structured as follows. A summary of related works is presented in Section 2. The proposed SPLITSnow model is described in Section 3. The evaluation framework employed in this research is then detailed in Section 4, with a discussion of *in silico* experimental results to follow in Section 5. Concluding remarks and directions for future work are outlined in Section 6. To facilitate the reader's understanding of the logical framework of this research, the technical objectives are outlined in Fig. 1.

2. Previous work

This section provides an overview of representative works on the modeling of snow reflectance using stochastic ray tracing methods, rather than deterministic methods employed to numerically solve related differential equations such as the DISORT model by Stamnes et al. (1988). The development of snow reflectance models is described in a manner that highlights the evolution of the various efforts over the previous few decades. The focus of this overview is on models primarily suitable for simulations of light interactions with snow in the visible and infrared domains. The reader interested in modeling efforts in the microwave domain is referred to a comprehensive work in this area by Picard et al. (2018).

We begin by identifying initial attempts to model snow reflectance using single scattering of spheres combined with analytical theory. Next, a selection of single-scattering models that made use of non-spherical shapes are presented, before continuing with multiple scattering models. These are subdivided into two categories: those based on a volume of modeled snow grains, and those that are based on

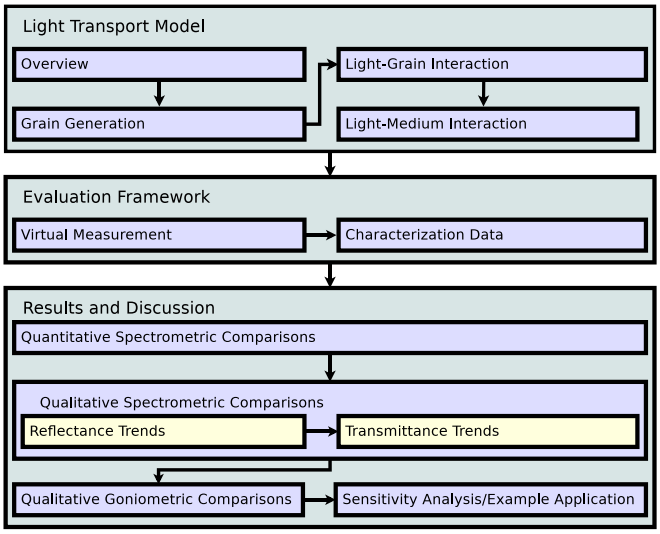

Fig. 1. Diagram illustrating the technical objectives outlined in subsequent sections of this work. First, the various components of the light transport model are presented. Second, the evaluation framework is discussed. Third, various *in silico* experimental results are presented that illustrate the predictive nature of the model.

tomographic scans of snow.

Due to computational time and memory limitations, many initial works focused on single-scattering and used the computed results as a phase function (Bohren and Huffman, 1983) to supplement a more complex, theoretical analysis. This archetypal method was demonstrated early by Bohren and Barkstrom (1974). Assuming a monodirectional source beam of radiation, they computed the single-scattering phenomenological coefficients required for an application of the Mie theory (Bohren and Huffman, 1983) using a single transparent sphere. Later, this was extended to account for snowpack depth to demonstrate a preferential absorption of longer wavelengths in the visible region (Bohren, 1983).

A transformative step in the paradigm was to consider nonspherical crystal shapes. Yang and Liou (1996) computed the phase function of hexagonal crystals using ray tracing, and compared its results to those obtained by using the finite difference time domain method (Gedney, 2011) on a similar crystal shape. The geometric ray tracing method was used for the near field and then transformed to the far field using a novel intensity mapping algorithm. This allowed them to extend their hybrid method to efficiently compute single-scattering albedo for small 3D ice crystals, that were close to the FDTD results. Grundy et al. (2000) performed a single-scattering simulation for arbitrary polygonal meshes. They focused on computing the single-scattering albedo, phase function, polarization and radiative transfer near the grain. They were also able to find an analytical approximation to the single-scattering phase function, using particle size, aspect ratio, and roughness as parameters. Recognizing the limitations of using "equivalent spheres" (Grenfell and Warren, 1999), Jin et al. (2008) investigated a variety of shapes and the effect that their different scattering phase functions had on bidirectional reflectance. They compared spheres, plates, column crystals and aggregates of columns. The results of these single-scattering simulations were input into a radiative transfer model and compared with measured data at 870 nm. This wavelength was chosen to avoid the influence of soot and liquid water content. A good agreement was obtained between the measured snow sample, and the simulated snow structure, thus demonstrating the degree of fidelity (Gross, 1999) that can be achieved by *in silico* investigations.

Barkstrom (1972) was an early advocate for multiple scattering models. His work used sphere-shaped snow grains to provide a quantitative argument to consider multiple scattering effects. Wiscombe and Warren (1980) provided an analytic model, based on Mie theory, that used the delta-Eddington approximation (Joseph et al., 1976) to account for multiple scattering. Their model also used spherical snow grains.

A number of attempts have since been made to simulate the 3D structure of snow grains in order to reproduce multiple scattering effects. These efforts focused on modeling the three dimensional structure of snow samples and then applying ray tracing to compute the scattering profiles. Kaempfer et al. (2007) tested two different snow representations. Their first attempt consisted of filling a volume with hemispherically-capped cylinders. This allowed for the testing of parameters such as grain size and pore space. Their second attempt recreated the microstructure of snow using an X-ray micro-tomography scan. This did not allow for parameter tuning. Instead, it provided a reconstructed representation of a particular snow sample. Bänninger et al. (2008) also used tomograph data to investigate biconical reflectance of snow with similar results, and found good agreement between measured and simulated reflectance. While Haussener et al. (2012) used tomograph data to develop a method for determining snow optical properties. Interestingly, their study provided evidence that employing a simplified morphology in a radiative transfer model will introduce significant errors in the visible and near infrared. The SnowRAT model developed by Picard et al. (2009) extended the filled volume strategy using a variety of different grain shapes such as spheres, hexahedra, cylinders and hyperboloids. These shapes, and aggregations of these shapes, were tested for their reflectance properties. In particular, the effect of snow grain shape on the specific surface area (SSA) to albedo relationship was investigated at 1310 nm. They demonstrated that, for example, cubic grains reflected approximately 40% more than spherical grains with the same SSA. Addressing the lack of readily available tomography data for snow, Xiong and Shi (2014) generated a Gaussian random field with a qualitatively similar structure to a tomograph (Xiong and Shi, 2014, 2017; Xiong et al., 2015). This structure was divided into ice and air by selecting a threshold value. Xiong and Shi (2018) later developed an algorithm to successfully determine snow SSA using their model.

In addition to the above, a multilayer model that investigated inhomogeneity of snowpack was implemented by Zhou et al. (2003). They determined that in the near infrared, a thickness of 5 cm is enough to be treated as semi-infinite. However, in the visible, a much larger depth is required.

The models discussed thus far have addressed the reflectance of dry snow. This impacts the results of the models since the optical properties of water differ from those of pure ice forming snow. In particular, the locations and magnitude of the extrema in the extinction coefficient (also known as the imaginary part of the complex index of refraction (Bohren and Huffman, 1983)) can vary between the two (see Fig. 5 in Section 4). The overall spectral reflectance is affected because snow may contain some water content, either as a vapor or in liquid form (Colbeck, 1982, 1997).

Using Mie theory, Green et al. (2002) attempted to determine the effect that water has on reflectance. In particular, they focused on the local minima in the extinction coefficients for ice and water which occur at 1030 nm and 980 nm, respectively. They demonstrated a shift of the absorption features centered at 1030 nm toward shorter wavelengths by representing snow grains as water-coated spheres.

Finally, it is worth noting that the importance of research initiatives for properly accounting for multiple scattering within snow deposits transcends spectral domains. For instance, Picard et al. (2018) has recently remarked that accurate simulations of microwave interactions with snow on the ground would require more advanced scattering models, which, in turn, would demand full three-dimensional representations of snowpack microstructure.

3. Light transport model

This section describes the formulation of the proposed model,

SPLITSnow. Section 3.1 provides an overview of the model. Details about the stochastic generation of individual grains are provided in Section 3.2. In Section 3.3, the simulation of light interactions with individual grains using geometric optics is described. Finally, light transport through the interstitial medium is discussed.

3.1. Overview

The proposed model employs a first-principles simulation approach. This approach is implemented using an algorithmic formulation based on the application of Monte Carlo methods (Hammersley and Handscomb, 1964) and ray optics concepts (Born and Wolf, 1999) as schematically depicted in Fig. 2. A light ray (or more concisely, a *ray*) travelling at a specific wavelength is directed toward the sample from the illumination source. The sample is bounded by both upper and lower planes. Within these planes a sequence of grains is instantiated and discarded, keeping only the currently active grain stored in memory. In the diagram depicted in Fig. 2, the black grain is the current one being examined by the simulation. The faded grains with solid outlines were completed and have been discarded. The faded grains with dashed outlines have yet to be instantiated. All grains are instantiated as needed, and their properties are all determined stochastically. This process is repeated to ensure the convergence of the radiometric quantities being estimated (Baranoski et al., 2001; Krishnaswamy et al., 2004).

Fig. 3 provides a high-level overview of the decision tree that a ray undertakes when interacting with the material. The incident ray is the input to the system. The first task is the process of particle generation. After particle generation, the ray is interacted with the pore space. This may entail the space between two particles, or the space between a

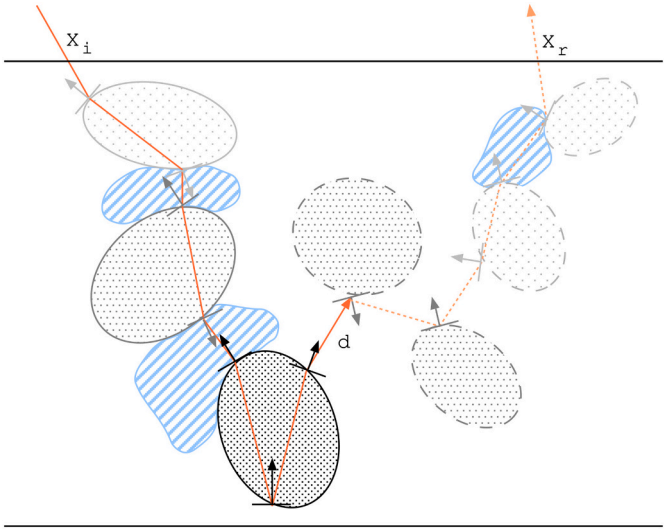

Fig. 2. Diagram illustrating the traversal of a ray through a given snow sample using the stochastic approach employed by the proposed model. After a ray enters the sample at the point X_i, a sequence of grains is randomly generated. Each grain is modeled as a prolate spheroid whose geometric properties are selected stochastically. The distance between grains, d, is also chosen at random based on the specified sample density, D. Grains that have been traversed are shown with a solid outline. Grains that have yet to be instantiated are shown with a dashed outline. Only one grain is required to be stored in memory at a time. This grain is shown with a solid black outline. To simulate the grains' facets, their normal vectors are perturbed using an appropriate probability distribution. Air is the default interstitial medium between grains. In this work, water may be used as a second medium. The fraction of pore space that is made up of water is specified as a model parameter. The presence or absence of interstitial water is decided using the water fraction as the probability. The ray's traversal is completed when it exits the sample at the point X_r. Alternatively, it can be terminated by an absorption event within the sample.

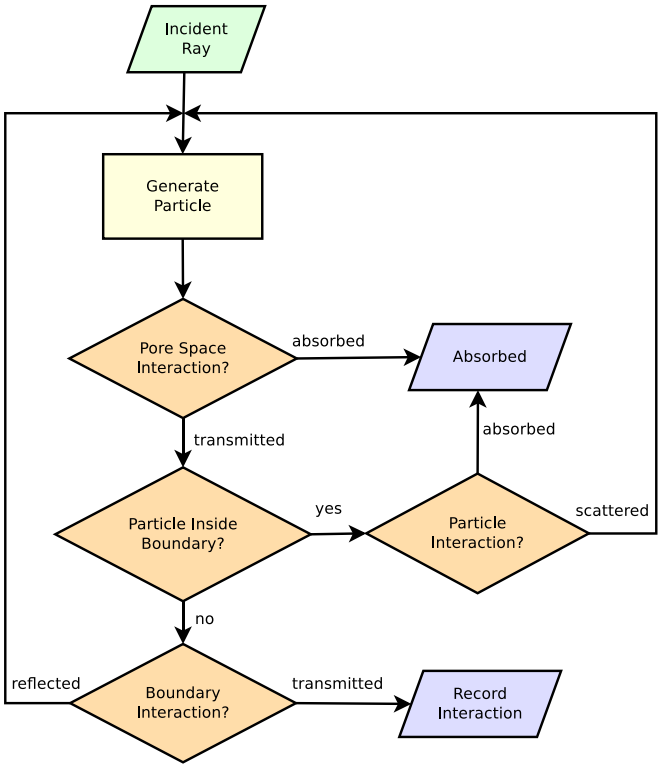

Fig. 3. Flow chart depicting the high-level decision tree that a ray undertakes when interacting with snow grains. Note the repetitive nature of the decision tree, whereby particles are generated on demand until the ray is either absorbed, or exits the material.

particle and the material boundary. If a newly generated particle is outside of the material boundary, then the ray interacts with the boundary, rather than the particle. Otherwise, the ray interacts with the particle.

As light first enters the sample, a random distance, d, to the first grain is computed by using:

$$d = -\overline{d} ln(\xi) \tag{1}$$

where $\overline{d}$ is the mean distance between grains, ln is the natural logarithm, and ξ is a uniformly distributed random variable in the range of $(0, 1)$. The mean distance between the grains is computed from the specified density, D, which is a model parameter. Technical details describing the method of computing the mean distance from density are provided in 7.

Once a distance is chosen, a grain and its geometric properties are then generated. These properties include the major and minor spheroidal axes, the entry point on the grain, and the normal vector at the intersection point. The grain is spatially translated so that the ray strikes the point of intersection precisely. These properties are all determined using specific probability distributions, which are discussed in Section 3.2. The ray is then refracted or reflected using the Fresnel coefficients (Pedrotti and Pedrotti, 1993) as the probability of success in a Bernoulli trial (Wasserman, 2004).

If the ray is reflected, then the grain is discarded. At this point, a new distance to the next grain is chosen using Eq. (1), and a another grain is generated with new properties using the same probability distributions. In addition, an interstitial medium is also selected probabilistically. The percentage of pore space that is composed of water is specified as a simulation parameter, and this percentage is used as the probability of success in a Bernoulli trial. In this way, the pore space is represented as either water or air by the SPLITSnow formulation.

If the light enters the grain, then it is refracted using the grain's index of refraction and extinction coefficient (Born and Wolf, 1999). These

(spectral) wavelength dependent quantities have distinct values for ice and water. The stochastically generated surface normal vector is used with these values to compute the ray's direction within the grain. Once within the grain, the ray may be transmitted or absorbed. To determine whether or not the ray is absorbed by the grain, the length traveled to the exit point and the grain's extinction coefficient are used to compute the probability in another Bernoulli trial. Should the ray be absorbed, it is discarded and a new ray is cast from the source. Otherwise, the ray reaches the exit point of the grain and Fresnel's laws are used once again to determine if the ray is internally reflected or refracted into the medium. A new normal vector is stochastically generated at the potential exit point for this purpose.

Internal reflection may continue until the ray is absorbed or exits the grain. In the former case, the grain is discarded. In the latter case, Eq. (1) is used to compute the distance to the next grain, and an interstitial medium is again probabilistically chosen. It is possible for the interstitial medium to absorb the ray. The distance and the extinction coefficient of the selected interstitial medium are used to probabilistically determine whether this occurs.

Should the ray reach either the upper or the lower bounding plane, then its position and direction of exitance are used to compute a BSDF reading. These readings are the outputs of the simulation. In this work, no boundaries are imposed on the horizontal dimensions. Consequently, samples are infinite in the x and y dimensions, but finite in the z-axis (depth).

There are a number of computational advantages to this approach. First, the amount of in-memory storage is drastically reduced since only one grain is kept at a time. However, eliminating the computational costs of traversing a complex search space provides an even greater benefit. Previous multiple scattering models required the storage of a multitude of grains. The real cost of this approach comes from searching through this set for the nearest grain. This requires computing the intersection of each grain with each ray, which can quickly become intractable. By contrast, the SPLITSnow stochastic approach only requires a small number of calls to a random number generator. A disadvantage of this approach is that once a ray exits a grain, it will never have the opportunity to interact with that grain again since it has been discarded. However, the computational efficiencies outweigh this consequence since the purpose is to aggregate the result of numerous samples for the purpose of Monte Carlo integration, and since macroscopic details are not modeled.

3.2. Grain generation

The SPLITSnow formulation is not dependent upon any particular grain shape. In this work, prolate spheroids are employed for consistency with the literature on snow deposits subject to morphological changes over time (Colbeck, 1982, 1997), commonly referred to as *faceted rounded particles* (Fierz et al., 2009). As described below, the SPLITSnow formulation allows crystalline features to be added to the spheroids in the form of microfacets (Torrance and Sparrow, 1967; Cook and Torrance, 1982). This representation allows for a variety of morphological ages to be investigated, which are more prevalently the object of geophysical investigations.

The geometric properties of each grain are generated stochastically (see Fig. 4). These properties include the size, shape, location and the microfacet at the point of intersection. The values assigned to the grains' optical properties, such as the index of refraction and the extinction coefficient for ice, were obtained from datasets available in the literature. The sources of these datasets are provided in Section 4.

The grain's semi-major axis, b, is a random variable with a uniform probability distribution that allows for a configurable range. Its sphericity, Ψ, is also a represented by a random variable based on a probability distribution suggested by Vepraskas and Cassel (1987). Inscribed circle sphericity (Riley, 1941) relates the overall shape of the grain to a perfect sphere. For a perfect sphere, Ψ is equal to one. Low values of Ψ lead to the generation of shapes that have a high eccentricity. The semi-major and semi-minor axes are related to Ψ through the following formula:

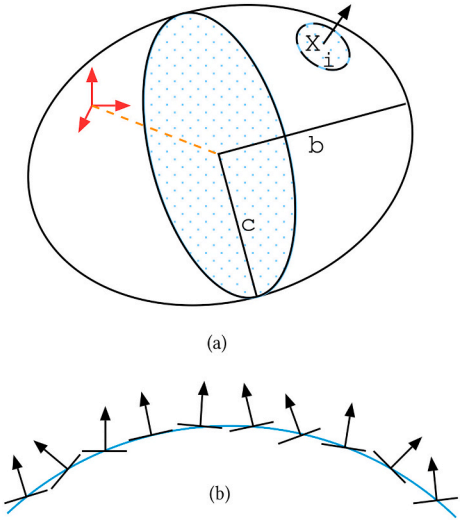

Fig. 4. Generated geometric properties of a grain. Diagram (a) depicts its axes and a stochastically selected intersection point on its surface. The semi-major axis, b, is chosen at random based on a uniform distribution. The semi-minor axis, c, is a function of b and the inscribed circle sphericity, Ψ, which is also a random variable (see Eq. (2)). The orientation of the semi-major axis is determined by selecting a uniformly distributed point on a sphere and orienting the axis in the direction of that point. The intersection point on the grain, X_i, is uniformly distributed on the spheroid. However, it is restricted to the side facing the incoming ray. The location of the grain is adjusted to ensure that X_i intersects the ray. The local origin of the grain is represented by the red axes, and the orange dashed line represents the particle's translation so that the ray intersects the grain at X_i. At X_i, the angle of the normal vector away from the orthogonal direction is perturbed using a normally distributed random variable. Diagram (b) illustrates how the surface details are represented as microfacets, which are associated with their specific normal vectors.

$$\Psi = \sqrt{\frac{c}{b}} \tag{2}$$

Eq. (2) can then be used to compute the semi-minor axis, c, from b and Ψ.

The orientation of the grain is stochastically chosen by uniformly selecting a point on the unit sphere and orienting the semi-major axis toward this point. The point of intersection with the grain is also distributed uniformly on the surface of the grain. However, it is restricted so that it must be facing the direction of the incoming ray. The grain is then repositioned so that the incoming ray strikes it at the stochastically selected point. Due to the stochastic nature of this process, it is possible that a grain is partially outside of the sample material boundaries when close to the upper or lower bounding planes. When this occurs, the grain is rejected and a new one is generated.

3.3. Light and grain interactions

When a propagating ray travelling at a wavelength λ interacts with a grain, it is probabilistically reflected or refracted based on the spectrally-dependent Fresnel coefficients (Pedrotti and Pedrotti, 1993). Therefore, to simulate the faceted features of a morphologically young ice crystal, its normal vector is perturbed at its faceted surface, as depicted in Fig. 4 (a), using a stochastic approach. More specifically, Fig. 4(a) shows the intersection point, X_i, on the surface of the spheroid. For the local area surrounding X_i, a new normal vector to the surface is stochastically generated as described below. This keeps the overall grain size consistent while allowing for more faceted forms. The result of this approach is

portrayed graphically in Fig. 4(b).

For a normal vector, $\vec{n}$, of the spheroid at hand, a perturbed normal vector, $\vec{n}'$, is computed using a random variable, ξ, that is normally distributed with a mean of zero by the formula:

$$\vec{n}\cdot\vec{n}' = 1 - |\xi| \tag{3}$$

The standard deviation of the normal distribution is defined as:

$$\sigma = \frac{\mathscr{F}}{2} \tag{4}$$

where $\mathscr{F}$ represents facetness, a tunable model parameter. More precisely, a facetness of zero yields a perfectly smooth spheroid. Using this stochastic method, both faceted crystals and rounded grains are represented efficiently, without the computational overhead of directly accounting for complex details on the grain's surface.

Fresnel coefficients are then used to determine the probability of reflection. A Bernoulli trial is performed using this probability to determine success. Upon success, the ray is reflected into a stochastically chosen interstitial medium (see Section 3.4). Otherwise, the general form of Snell's law that makes use of both the grain's index of refraction and the extinction coefficient is used to determine the ray's angle of refraction into the grain (Born and Wolf, 1999).

We remark that ice crystals are known to be only slightly birefringent (Warren, 1984), and that their index of refraction does not vary significantly with their orientation. Furthermore, to the best of our knowledge, the existing hyperspectral refractive index datasets provided in the literature for the wavelengths under investigation (*e.g.*, Warren and Brandt (2008)), do not provide data for parallel *vs.* perpendicular orientations of electromagnetic waves through ice. As a consequence, polarization effects are not accounted for in the current formulation, and are left for future study.

Diffraction effects are also not considered since the wavelengths of light used in this investigation are considerably shorter than the separation between the snow grains. The maximum snow density considered in this work is 450 kg m^{-1}. Choosing this density yields the smallest mean distance between snow grains, which computes to roughly 4.3×10^{-4} m. (See 7.) The longest wavelength of incident radiation considered in this work is 2500 nm, or 2.5×10^{-6} m, which is two orders of magnitude smaller than the smallest mean distance. Furthermore, the grain shapes considered are spheroidal, and thus the apertures between grains generally do not form rectangular patterns with the aperture lengths being significantly greater than their widths — a geometry which is commonly associated with diffraction effects (Pedrotti and Pedrotti, 1993).

Within the snow grain, the possibility exists that the ray will be absorbed. The probability of absorption depends upon the length of the path the ray travels through the grain. The exit point out of the grain is computed geometrically as a ray-object intersection. The distance traveled within the grain, d, along that path is thus computed as the length along the ray between the point of incidence and the point of (potential) exitance. The probability of absorption, a, is a function of this distance, and it is given by:

$$a(\lambda) = e^{-\alpha(\lambda)d} \tag{5}$$

where the absorption coefficient is computed as:

$$\alpha(\lambda) = \frac{4\pi k(\lambda)}{\lambda} \tag{6}$$

with $k(\lambda)$ representing the extinction coefficient at the wavelength λ for ice (Bohren and Huffman, 1983).

3.4. Light propagation through the interstitial medium

When the ray is propagated through the interstitial medium, either because it has been reflected off a grain, or because it has exited a grain, the optical effects of the interstitial medium must be taken into account. The SPLITSnow formulation allows for any number of media to be present in the interstitial (pore) space between grains. However, for the purpose of simulating light interaction with snow, only two media are considered. These are water and air.

The default interstitial medium between the snow grains is air. The fraction of pore space that is made up of water is specified as a model parameter. When the ray enters the pore space, the presence or absence of water is decided using the water fraction as the parameter of success in a Bernoulli trial. If water is chosen, then the entire pore space up to the next grain is assumed to be water. Otherwise, the entire pore space is assumed to be air.

The distance to the next grain, d, is stochastically determined using Eq. (1) as described in Section 3.1. Similar to a ray interacting with a grain, a ray traversing the interstitial medium may be absorbed within it, with the probability of absorption being also computed using Eq. (5). If the ray is absorbed, then a new ray is cast and the process begins again. Otherwise, a new grain is generated as described in Section 3.2. The index of refraction and the extinction coefficient of the current medium are used when computing the Fresnel coefficients and employing Snell's law to obtain the direction of propagation of rays interacting with individual grains (Section 3.3).

4. Evaluation framework

As mentioned earlier, models based on different design approaches (*e.g.*, deterministic or stochastic) can be used in the analysis of data obtained through *in situ* experiments. For instance, to complement their analysis, Gergely et al. (2010) used the DISORT model first presented by Stamnes et al. (1988) to complement their analysis of the relationship between transmittance and snow specific surface area. Also, it is not unusual to compare predictions provided by new models with simulated readings obtained using existing models, particularly when reliable ground truth data is not available. We remark that reliable measured radiometric data for snow, albeit from a moderate number of sources, is available in the literature. Moreover, comparisons of results provided by different models may be more susceptible to biases associated with the assumptions considered in the design of those models. For these reasons, we believe that, as in any effort in physical sciences, the ground truth to be used in the evaluation of a novel light transport model should be actual experimental data. Accordingly, we have elected to evaluate the predictions made by the proposed stochastic SPLITSnow model through quantitative and qualitative comparisons with measured data and experimental observations reported in the literature, including the dataset provided by Dumont et al. (2010). In this section, we describe the framework used to carry out these comparisons.

4.1. Virtual measurement procedures

As discussed in Section 3, an *in silico* experiment is executed by casting rays into a digital representation of the selected snow sample. Once the ray has escaped from the sample, the exitance details are recorded using a virtual goniophotometer (Krishnaswamy et al., 2004). With this procedure, the hemispherical radiometric responses resulting from light interactions with the snow grains are quantifiable in terms of BSSRDF since all geometric values, including positions, of the incidence and exitance points are known. To enable comparisons with BRDF data reported in the literature, the separation between incidence and exitance points can be assumed to be negligible so that the model predictions can also be expressed in terms of BRDF (Nicodemus et al., 1977).

Considering the directional outputs of the simulation, the sensor of this virtual goniophotometer is divided into regions of equal solid angle. Since the incident ray is directional, a directional-conical reflectance experiment is undertaken with this type of virtual device. At each de-

tector, the ratio of rays observed to rays cast is divided by the projected solid angle, yielding the BRDF (and, by analogy, the BTDF). By decreasing the solid angle of the virtual collectors, better approximations to the true BRDF are achieved at the expense of additional computational cost. Thus for each wavelength, λ, the BRDF is numerically computed as follows:

$$f_r(\theta_i, \phi_i; \theta_r, \phi_r; \lambda) = \frac{n_\lambda(\theta_r \phi_r)}{N_\lambda} \cdot \frac{1}{\Omega_r} \left[\mathrm{sr}^{-1}\right] \tag{7}$$

where $n_\lambda(\theta_r, \phi_r)$ is the number of rays striking the collector in the reflected direction on the virtual goniophotometer, N_λ is the total number of rays cast, Ω_r is the projected solid angle of the collector, and (θ, ϕ) represent the locations in spherical coordinates.

Directional-hemispherical reflectance is a variation of the directional-conical reflectance where the entire upper hemisphere is used as a single detector. Thus, the sum of the contributions of each detector is equal to the sum for the total upper hemisphere. Hence, the directional-hemispherical reflectance can be numerically computed as:

$$\rho(\theta_i, \phi_i; \lambda) = \frac{1}{N_\lambda} \sum_{\theta,\phi} \frac{n_\lambda(\theta_r, \phi_r)}{\Omega_r} = \frac{n_\lambda}{\pi N_\lambda} \tag{8}$$

where n_λ is the total number of reflected rays in all directions of the upper hemisphere.

4.2. Material characterization data

For evaluation purposes, several model parameters are subject to variation. These include grain size, facetness and density. More specifically, *in silico* experiments are conducted by varying the individual parameters, which are assessed against the expected effects on reflectance and transmittance as reported in the literature.

In addition to snow grain characterization, we also investigated the effects of water content, as it has an application in determining near-surface water saturation of snowpack for remote sensing (Green et al., 2002; Dozier and Painter, 2004). We also considered geometric aspects, including snowpack depth, and the angles of incidence and exitance. Each experiment is hyperspectral in nature so that a thorough dataset of results is accumulated to be analyzed.

Grain size is the most predominantly studied snow grain characteristic discussed in the literature since it has a significant effect on reflectance (Nolin and Dozier, 1993, 2000; Nakamura et al., 2001; Green et al., 2002; Jin et al., 2008; Lyapustin et al., 2009). As grain size decreases, reflectance is known to increase (Bohren and Barkstrom, 1974; Nakamura et al., 2001). However, additional snow grain characteristics are utilized to achieve a better fit with the measured reflectance data of snow samples. For example, we conducted experiments to determine the set of parameter values required to match reflectance measurement values reported in the literature by Dumont et al. (2010). The model parameter values employed to obtain these results are presented in Table 1. The parameter values specified in Table 1 were determined by iteratively exploring the model parameter space. Values in the top portion of the table represent those that were explored experimentally to achieve the closest congruence with measured data. Values in the lower section of the table were directly stated by Dumont et al. (2010). In our simulations, we considered a spectral resolution of 10 nm, which is sufficient to describe spectral features present in the actual measured data captured using a coarser resolution. We also investigated similar spectrometric trends regarding transmittance and qualitatively compared the results to trends that are reported in the literature.

We also investigated the effect of model parameters on BRDF trends. We qualitatively compared predictions made by changes in grain size and facetness with trends that have been reported in the literature. In addition to this, we test the effect of varying the angle of incidence and the wavelength of the illumination source. The predictions made by these experiments were also qualitatively compared to trends described in the literature.

Table 1
SPLITSnow parameters employed in the characterization of the snow sample considered in the *in silico* experiments described in this work. Values used in the upper section were found through parameter exploration. Values in the lower section correspond to the snow sample used in the actual experiments (Dumont et al., 2010).

Parameter	Value	Units
Particle size minimum	300	[μm]
Particle size maximum	750	[μm]
Water saturation	5	
Facetness minimum	0.2	
Facetness maximum	0.4	
Facetness mean	0.3	
Facetness standard deviation	0.072	
Sphericity minimum	0.6	
Sphericity maximum	0.95	
Sphericity mean	0.798	
Sphericity standard deviation	0.064	
Density	0.275	[g cm^{-3}]
Temperature	−1	[°C]
Sample depth	12	[cm]
Polar incidence angle	0°	
Wavelength range	400–2500	[nm]

Note that for spectral studies of reflectance and transmittance, we used the incident angle of 0° as specified in Table 1. Although observations of snow with a solar zenith angle of 0° are uncommon in nature, we remark that controlled studies of spectral reflectance and transmittance trends of particulate materials often use this angle of incidence. (For example, see Nakamura et al. (2001), Bänninger and Flühler (2004), Ciani et al. (2005), and Dumont et al. (2010).) However, when investigating directional trends, it is more common to find studies in the literature where the angle of incidence is varied. We followed this technique of varying the angle of incidence when making comparisons to trends observed with a directional component.

While *in situ* and laboratory experiments that quantify directional reflectance data are fundamentally important, sometimes there are geometric limits on the incidence and reflectance angles to be measured depending upon the apparatus design. With an *in silico* experiment, there are no such limitations. Furthermore, the effectiveness-to-cost ratio of investigations can be improved by pairing traditional and *in silico* experiments since the latter enables a precise control of the parameters under study. However, while distinct polar incident angles are considered in this investigation, we fixed the azimuthal angle at 0°. We remark that SPLITSnow is a local light interaction model. Accordingly, macroscopic features, like sastrugi (Hudson et al., 2006) or wind effects (Middleton and Mungall, 1952), that can lead to an azimuthal asymmetry of light propagated by snowpacks covering relatively large areas, are outside our current scope of simulations.

We also remark that the spectral indices of refraction and extinction coefficients of water and ice are incorporated in the formulation of the SPLITSnow model (Section 3). Thus, in our simulations, we employed spectral curves (Fig. 5) obtained from the literature on these optical properties of water (Hale and Querry, 1973; Palmer and Williams, 1974; Pope and Fry, 1997; Wagner et al., 2000) and ice (Warren and Brandt, 2008).

We quantitatively compared directional-hemispherical spectral responses obtained using the SPLITSnow model with conical-hemispherical responses measured by Dumont et al. (2010). It is worth noting that Dumont et al. (2010) chose to perform the bulk of their analyses on their sample 3 which, according to them, provided results representative for their other samples. Therefore, we evaluated SPLITSnow simulated results through comparisons with measurements obtained from this sample, which we will refer to as the *representative sample* in the remainder of this work.

The representative sample was described as being “new wet snow” with “melt-freeze crusted grains” at the surface and “rounded particles”

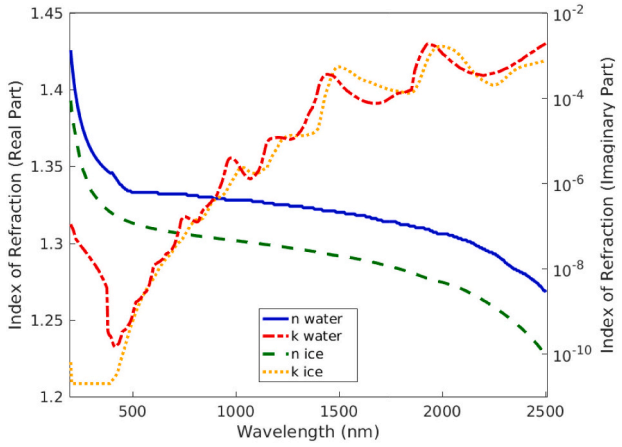

Fig. 5. Complex index of refraction curves for both water (Hale and Querry, 1973; Palmer and Williams, 1974; Pope and Fry, 1997; Wagner et al., 2000) and ice (Warren and Brandt, 2008) used in this work. The real part of index of refraction for water and ice are denoted by blue and green lines respectively. The imaginary part of the index of refraction for water and ice are denoted by red and orange lines respectively. The vertical scale for the real part of index of refraction is linear, while the vertical scale for the imaginary part of the index of refraction is logarithmic. (For interpretation of the references to colour in this figure legend, the reader is referred to the web version of this article.)

throughout its depth. The density was not measured. For their analyses of reflectance, Dumont et al. (2010) used values such as 0.1, 0.4, and 1 mm for the average grain size which they describe as being representative. The sample container was cylindrical with a 15 cm radius and 12 cm depth. However, they used a cuboid sample holder that was 16.5 cm deep to determine their radiometric bottom losses, which were found to be less than 1%. Since transmittance is also an output from the SPLITSnow model, we compared these transmittance simulation results with the expected bottom losses proposed by Dumont et al. (2010).

In addition to these quantitative comparisons, we qualitatively evaluated the SPLITSnow model by examining the impact that various snow grain characteristics have on simulated results. More specifically, we compared model predictions with experimental observations reported in the literature. For example, experimental evidence suggests that reflectance decreases as grain size increases (Nakamura et al., 2001).

Experimental studies of transmittance of light through snow are scarce in the snow literature (Beaglehole et al., 1998; Gerland et al., 2000; Perovich, 2007). This scarcity could be due to the fact that measurements of transmittance are difficult (Giddings and LaChapelle, 1961)] or because the insertion of a measurement device alters the radiation in the vicinity of the of the instrument (Dunkle and Bevans, 1956). It could also be due to the focus on remote sensing applications of optically thick snowpack (*e.g.*, Kim et al. (2019)). To our knowledge, the transmittance studies available in the literature were all performed in the field, and were affected by impurities (Perovich, 2007), morphological changes and snow melt (Gerland et al., 2000) or variations in solar radiation (Beaglehole et al., 1998). However, as noted by Bänninger and Flühler (2004), there are optical similarities between snow and other granular materials. As such, the effects of varying particular snow grain characteristics on transmittance for snow can be assessed by examining the transmittance profiles of other granular materials (*e.g.*, sand) from a qualitative perspective. For example, as the thickness (depth) of the deposits of these materials increases, the transmittance decreases (Bänninger and Flühler, 2004; Ciani et al., 2005); as grain size increases, the transmittance increases (Tester and Morris, 1987; Bänninger and Flühler, 2004; Ciani et al., 2005); and as porosity increases (*i.e.*, density decreases), the transmittance increases (Woolley and Stoller, 1978; Ollerhead, 2001). Accordingly, we performed transmittance experiments in which we assess the proposed model's predictive capabilities with respect to these aspects.

The incorporation of facets in the formulation of the proposed model allows it to efficiently represent complex grain features, which are relevant (Dozier and Painter, 2004) when considering the angular details of snow reflectance for remote sensing (Jiao et al., 2019). We performed *in silico* goniometric reflectance experiments, which we qualitatively compared with field observations reported in the literature, to illustrate this aspect. For example, a decrease near nadir and an increase in forward direction (with respect to the scattering limb) are observed in the simulated results. Both effects are described in the literature (Knap and Reijmer, 1998; Hudson et al., 2006; Dumont et al., 2010). An increased incident polar angle is associated with a stronger forward peak (Middleton and Mungall, 1952; Hudson et al., 2006; Dumont et al., 2010). Finally, smaller grains exhibit a stronger forward peak when compared to larger grains (Dumont et al., 2010).

In this work, the only snow temperature considered is −1 °C since the temperature of snow is typically near its melting point (Fierz et al., 2009). Furthermore, simulations in which we varied only the ice temperature in the range of −40–0 °C showed little difference in reflectance.

We have made the SPLITSnow model available for online use (both spectrometric (Natural Phenomena Simulation Group, 2020b) and goniometric (Natural Phenomena Simulation Group, 2020a) versions) to enable the reproduction and extension of the *in silico* experiments performed during this research. Its deployment was carried out using a model distribution framework (Baranoski et al., 2012) designed for this purpose. The default values assigned to the snow characterization parameters depicted on the model's webpage correspond to those used to obtain the results presented in this work (Section 5). However, a variety of reasonable values are permitted for characterizations suitable for the assessment of different phenomenological observations.

5. Results and discussion

In this section, we compare the simulated results generated by the proposed SPLITSnow model with measured hyperspectral reflectance data provided by Dumont et al. (2010). We also present the results of our experiments that predict spectrometric reflectance and transmittance trends, and compare these to measured trends that have been previously reported in the literature. We then provide our experimental simulation results that make predictions of goniometric trends and compare our simulation results with the measured responses reported in the literature. Next, we present a brief input-sensitivity analysis of the parameters discussed in this work. Finally, we describe an example application of the proposed model to study remote observations.

5.1. Quantitative spectrometric comparisons

Fig. 6 presents a graph depicting a comparison of model predictions with measured data provided by Dumont et al. (2010) considering an angle of incidence of 0°. As mentioned earlier, a detailed characterization of the grain size for the representative sample was not provided by Dumont et al. (2010) along with their data. However, in their own comparisons to previous models, they used average grain sizes ranging from 0.1–1 mm, and stated that their own "grain size measurements are too rough to be suitable as inputs." Furthermore, based on the description of their samples, it has been inferred that the selected sample's grains are within this range.

As it can be observed in Fig. 6, a close match has been achieved for reflectance throughout the entire measured spectrum (400–2500 nm). The computed root mean square error between the two curves is 0.0177. It has been noted by Jacquemoud et al. (1996), that root mean squared errors below 0.03 indicate good spectrum reconstruction, notably for remote sensing applications. In addition, note that prominent extrema are aligned. In particular, alignment is observed at the 1030 nm extrema. This suggests that the fraction of the pore space occupied by

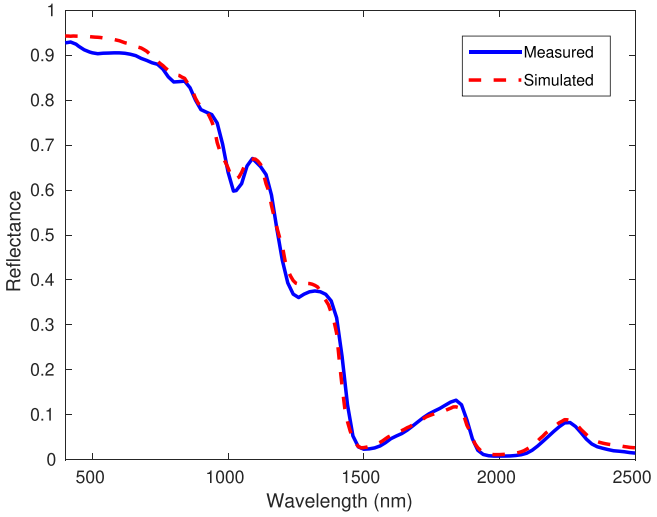

Fig. 6. Comparison of measured (Dumont et al., 2010) and simulated directional-hemispherical reflectance curves. The simulated curve was obtained using the SPLITSnow model and the sample characterization data provided in Table 1.

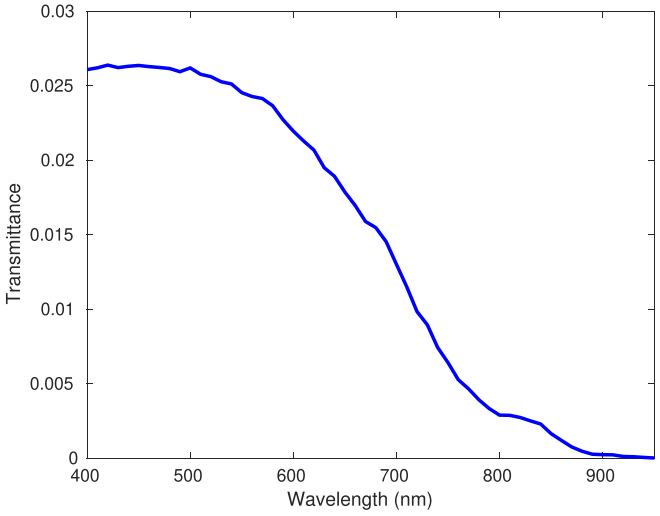

Fig. 7. Simulated directional-hemispherical transmittance curve computed using the SPLITSnow model and the sample's characterization dataset provided in Table 1.

water that was used in the simulation (5%) is representative of the residual water in the representative sample (Green et al., 2002).

As described in Section 3, facetness is a unitless parameter that is used to model the fine details of the grains' rough surface. The characterization of the sample employed by Dumont et al. (2010) indicates that it consisted of "rounded grains with mixed forms." Based on this description, the exploration of the parameter space focused on rounded grains. Best results were obtained using a normal probability distribution with a mean facetness of 0.3 and a standard deviation of 0.072. These values produce mostly rounded grains with some facets in the SPLITSnow formulation.

The differences between the measured and simulated curves are more pronounced in the 400–800 nm region of the spectrum. There is a number of possible explanations for these differences. First, relatively small amounts of impurities, as low 1 part per million, can reduce hemispherical reflectance by 5–15% (Warren and Wiscombe, 1980). Although Dumont et al. (2010) stated that their representative sample was taken from a relatively isolated location, they did not rule out the presence of contaminants from nearby sources (*e.g.*, vehicular traffic) or deposited from atmospheric air currents, that could have affected the measurement results. Second, we remark that in the absence of precise information, the values assigned to a number of the sample characterization parameters correspond to average data provided in the literature.

Fig. 7 displays the simulated transmittance results. The wavelength domain is only shown from 400 to 950 nm since transmittance values at higher wavelengths were all computed to be zero. As discussed in Section 4, the depth of the representative sample was 12 cm. However, their estimate of radiometric bottom loss, less than 1% using a 630 nm source of illumination, was performed on a sample with a depth of 16.5 cm. Since a good match was obtained considering simulated results that used a 0.3–0.75 nm grain size distribution, this range was used to assess the fidelity of the transmittance predictions. As it can be observed in Fig. 7, a maximum of 2.6% of the incident light is transmitted at the blue end of the spectrum (400–500 nm). The extinction coefficients associated with this band are lower than the extinction coefficient at 630 nm. Thus, as expected, the 2.6% loss resulting from our *in silico* experiment is on the same order of magnitude of that observed in the actual experiments (1%).

5.2. *Qualitative spectrometric comparisons*

5.2.1. *Reflectance trends*

In addition to the *in silico* experiments described in the previous section, we carried out three others to ensure that the predictions provided by the proposed model are consistent with observations described in the literature. Unless otherwise stated, all parameter values correspond to those depicted in Table 1, except for the independent variable under test.

The first experiment addressed the effect of grain size on reflectance. Fig. 8 shows the results. Reflectance was computed for four different mean grain sizes. The reported mean grain sizes are all chosen to be the center of a uniform distribution within a range of ±50 μm. As reported in the literature (Nakamura et al., 2001), reflectance decreases as grain size increases. This behavior is observed in the modeled curves presented in Fig. 8. Sensitivity to grain size is the lowest in the visible, and prominent in the 700–1300 nm band as expected (Nolin and Dozier, 1993). Furthermore, the effect of the absorptance minima of ice (Warren and

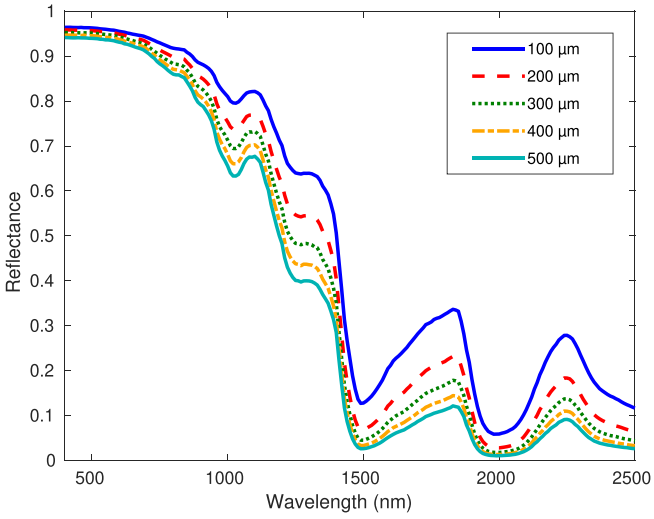

Fig. 8. Simulated directional-hemispherical reflectance curves computed using the SPLITSnow model considering various sizes of snow grains (100–500 μm) and an angle of incidence of 0°. The remaining sample characterization parameter values are provided in Table 1.

Brandt, 2008) at 1800 nm and 2250 nm can also be observed in the modeled curves depicted in Fig. 8.

The second experiment addressed the effect of facetness on reflectance. We remark that a low facetness represents a grain whose surface has few crystalline features, with a facetness of zero yielding a perfectly smooth grain. A high facetness characterizes a grain whose surface has many fine details.

Precipitated snow will undergo a morphological process that erodes the facets and leaves rounded grains (Colbeck, 1982). Fig. 9 demonstrates the effect of facetness on reflectance. This experiment shows that an increase in facetness will increase the total reflectance. Note that the 700–1300 nm band that is affected by grain size (Nolin and Dozier, 2000) is also affected by the microstructure of the grains. The 1800 nm and 2250 nm peaks exhibited in the infrared are similarly affected. These trends demonstrate the importance of accounting for grain facets in the formulation of a model for snow reflectance. In particular, any attempt to estimate grain size from reflectance (*e.g.*, Nolin and Dozier (2000)) can be improved by also examining the effect of facetness at these peaks.

Our third experiment investigates the effect of density on reflectance. Reflectance is known to be weakly dependent upon snowpack density when the depth is effectively semi-infinite. Bohren and Beschta (1979) observed a reflectance variation of less than 1% after compaction in the 350–2800 nm range. Our *in silico* spectrometric reflectance experiment reproduces this result. Using the parameters from Table 1 with the minimum (300 kg m^{-3}) and maximum (450 kg m^{-3}) densities reported by Bohren and Beschta (1979), the difference between the two reflectance curves are presented in Fig. 10. The root mean square error is less than 0.007 and the mean percent difference is 2.0%, which is similar in magnitude to the experimental results obtained by Bohren and Beschta (1979).

5.2.2. Transmittance trends

The presence of a trace amount of snow covering remote sensing targets can be sufficient to affect the detection and interpretation of their spectral signatures. Hence, it is important to evaluate the predictive capabilities of the SPLITSnow model with respect to light transmitted through snow layers. This was carried out through four *in silico* transmittance experiments, whose results we qualitatively compared with field observations reported in the literature, to illustrate this aspect.

Since studies of snow transmittance are scarcer than those performed on reflectance, we performed comparisons of model predictions with qualitative trends reported for other granular materials, such as sand-textured soils, in the literature. There are known phenomenological similarities between sand-textured soils, made up of quartz crystals, and snow, made up of ice crystals, with respect to radiant transfer at wavelengths sufficiently shorter than the size of the grains (Bänninger and Flühler, 2004).

Unless otherwise noted, the experiments described in this section employ the characterization parameter values of the representative sample presented in Table 1. In all experiments, the sample depth has been adjusted to 2 cm, except where depth is used as the independent variable. Note that the experiments in this section are restricted to the 400–1420 nm band since transmittance values at wavelengths higher than 1420 nm were all computed to be zero due to the strong absorptance of snow constituent materials, notably, ice and water, in the infrared domain.

In our first transmittance experiment, whose results are presented in

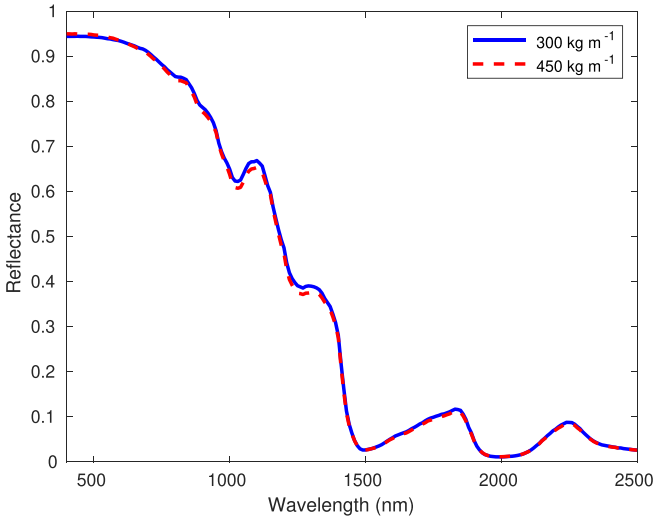

Fig. 10. Simulated directional-hemispherical reflectance curves computed using the SPLITSnow model considering two different densities (300 and 450 kg m^{-1}) and an angle of incidence of 0°. The remaining sample characterization parameter values are provided in Table 1.

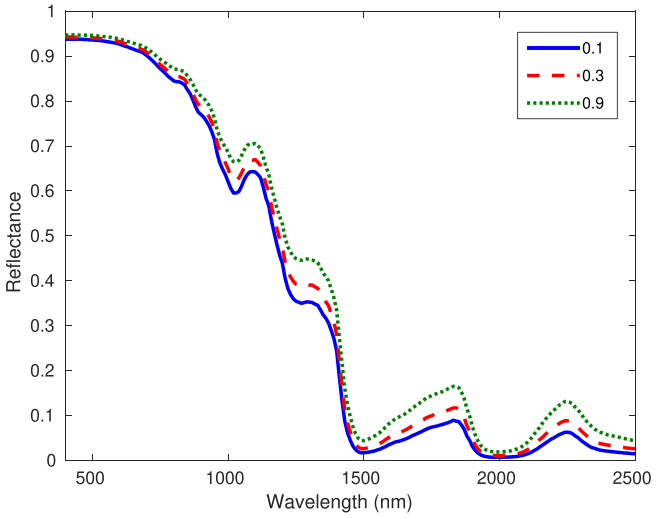

Fig. 9. Simulated directional-hemispherical reflectance curves computed using the SPLITSnow model considering various degrees of facetness (0.1–0.9). and an angle of incidence of 0°. The remaining sample characterization parameter values are provided in Table 1.

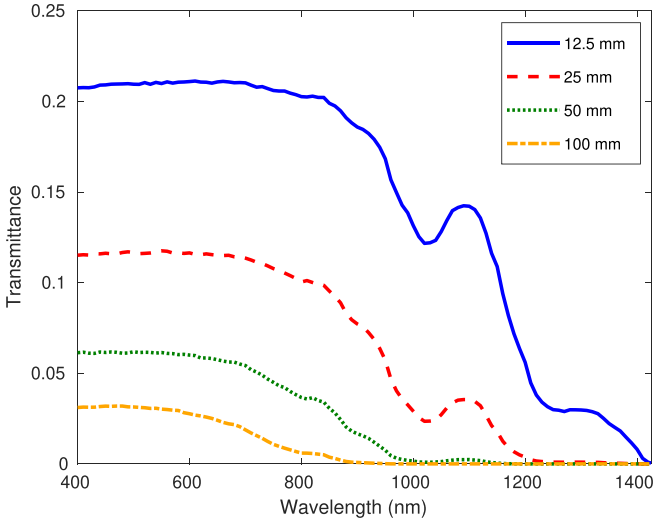

Fig. 11. Simulated directional-hemispherical transmittance curves computed using the SPLITSnow model considering various sample depths (12–100 mm) and an angle of incidence of 0°. The remaining sample characterization parameter values are provided in Table 1.

Fig. 11, we addressed the effect of sample depth on transmittance. As described in the literature (Bänninger and Flühler, 2004; Ciani et al., 2005), when the sample depth increases, the transmittance decreases. Note that the sample depth is doubled from one experimental instance to the next and the corresponding transmittance curves are approximately halved in the visible range (400–700 nm). We remark that there is a low amount of absorptance of ice in this band (see Fig. 5). However, where there are local maxima in absorptance, there is an even greater decrease in transmittance. For example, the absorption maxima at 1030 nm (Fig. 5, orange dotted line) corresponds to the minima in the transmittance.

In our second transmittance experiment, whose results are presented in Fig. 12, we addressed the effect of grain size on transmittance. As reported in the literature (Tester and Morris, 1987; Bänninger and Flühler, 2004; Ciani et al., 2005), transmittance is correlated with grain size, *i.e.*, as the grain size increases, the transmittance also increases. Larger grains, while being more absorptive, are also known to decrease the amount of scattering (Ciani et al., 2005). The resulting effect is that the absorption-to-scattering ratio is increased, which increases the depth that light penetrates into the material.

In our third transmittance experiment, whose results are presented in Fig. 13, we addressed the effect of water content. We note that the addition of water to sand-textured soils is known to significantly affect the qualitative trends observed in their measured transmittance spectra (Woolley and Stoller, 1978; Bliss and Smith, 1985; Tester and Morris, 1987; Ciani et al., 2005; Tian and Philpot, 2018). For translucent sand-textured soils, Woolley and Stoller (1978) and Bliss and Smith (1985) observed that as water saturation increases, transmittance also increases. However, for dark soils, they measured a decrease in transmittance as water saturation increased. This is explained by the increase in absorption (Tester and Morris, 1987). These trends are both visible in our simulation results presented in Fig. 13. In the visible spectrum (400–700 nm), ice grains are translucent and transmittance increases as saturation is increased, which matches the trend reported by Woolley and Stoller (1978) and Bliss and Smith (1985) for translucent materials. However, in the 800–1450 nm band, where there is an increase in absorptance (see Fig. 5), snow behaves like a “dark” material and the trend is reversed. This also matches the experimental observations reported by Woolley and Stoller (1978) and Bliss and Smith (1985) with respect to light transmission through particulate materials.

The final transmittance experiment investigates the effect of density.

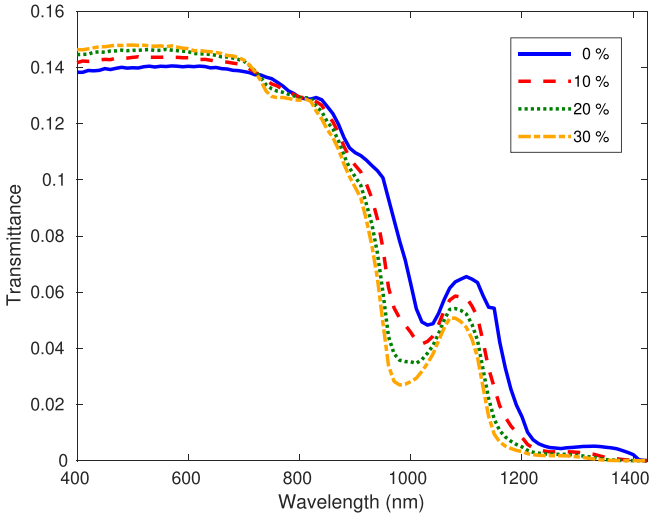

Fig. 13. Simulated directional-hemispherical transmittance curves computed using the SPLITSnow model considering various water fractions (0–30%), an angle of incidence of 0° and a sample depth of 2 cm. The remaining sample characterization parameter values are provided in Table 1.

For optically thin snowpack, density affects how light is transmitted to the underlying surface, which can affect estimates of snow cover in remote sensing applications (Hall and Riggs, 2007). Fig. 14 depicts the results of the experiment. As the density increases, the transmittance decreases as expected for particulate materials (Woolley and Stoller, 1978; Ollerhead, 2001). An increase in density affects the light propagated through a snow deposit as it allows for more absorptions and scattering events. The net impact of these effects is a reduction in transmittance.

5.3. *Qualitative goniometric comparisons*

In this section, we qualitatively compare goniometric simulated results with phenomenological traits observed in goniometric measurements reported in the literature. In addition to these qualitative comparisons, we also present the results of two *in silico* experiments on the effects of different grain characteristics on directional reflectance.

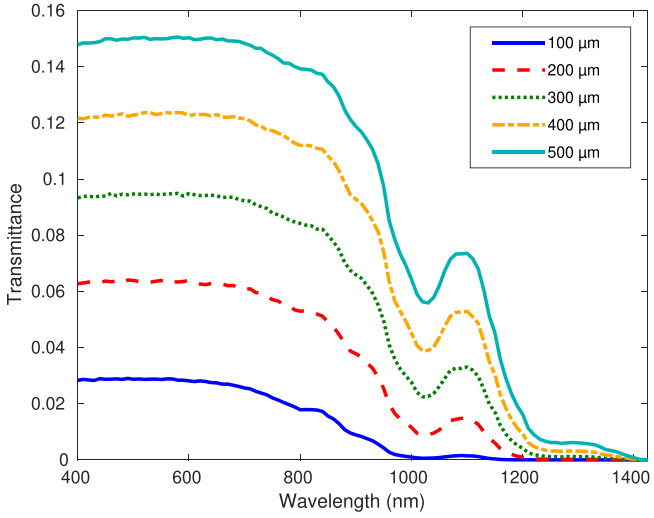

Fig. 12. Simulated directional-hemispherical transmittance curves computed using the SPLITSnow model considering various sizes of snow grains (100–500 µm), an angle of incidence of 0° and a sample depth of 2 cm. The remaining sample characterization parameter values are provided in Table 1.

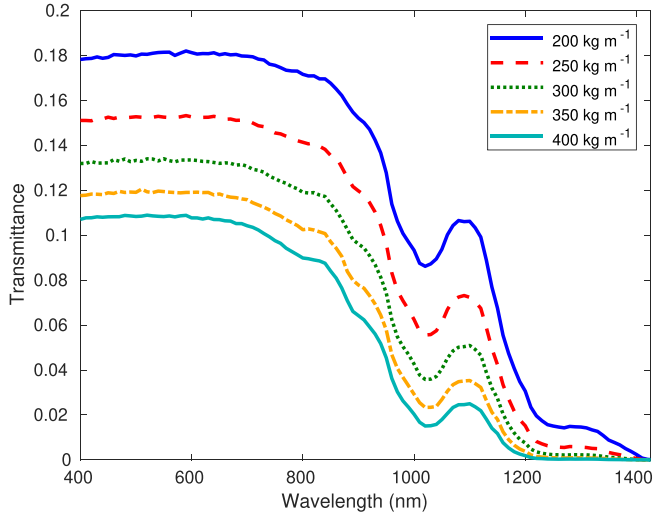

Fig. 14. Simulated directional-hemispherical transmittance curves computed using the SPLITSnow model considering various densities (200–400 kg m^{-3}), an angle of incidence of 0° and a sample depth of 2 cm. The remaining sample characterization parameter values are provided in Table 1.

Initially, we present a qualitative comparison to measured data provided by Dumont et al. (2010). For all three angles of incidence we have shown that the qualitative trends exhibited in the measured data are reproduced by simulation. However, the forward-scattering limb was more pronounced in the measured data when the angle of incidence was 60°. This may be due to differences between the characterization values employed in the simulation and the representative sample. In Fig. 15, we show the most representative case which utilizes a 30° incident angle. This figure presents both a simulated BRDF plot through the principal plane (blue curve) and measured values provided by Dumont et al. (2010) (blue squares). The angle of incidence (30, black line) is the same for both measured and simulated values.

Fig. 16 presents simulated BRDF plots obtained for the representative snow sample considering three (polar) angles of incidence. Each plot corresponds to reflectance values taken through the principal plane that contains the incident ray and the normal vector to the sample at the point of illumination. In their field study, Hudson et al. (2006) described two main features which are also reproduced by these simulated results. First, the reflectance values measured for reflection angles close to the zenith were lower than those measured for reflection angles close to the horizon. Second, this phenomenon becomes more noticeable for larger angles of incidence. Both features can be observed in the plots depicted in Fig. 16.

Fig. 17 presents a simulated BRDF plot obtained considering a wavelength of 1800 nm and an angle of incidence of 69.3°. Notice that in addition to the features outlined above, a reduction in the reflectance values (represented by a concave shape) near the zenith can be observed. This distinct darkening feature is apparent in the measured data obtained by Hudson et al. (2006) for the same wavelength and incident angle. Dumont et al. (2010) also observed this feature in their measured data, which they deemed "nadir darkening."

Fig. 18 presents simulated BRDF plots obtained considering the same angle of incidence (69.3°) and using two wavelengths (600 and 1800 nm) associated with markedly distinct spectrometric reflectance values. The red dashed curve is reproduced from Fig. 16, and the blue solid curve is reproduced from Fig. 17. For illustrative purposes, both curves in Fig. 18 are presented using the same scale. As it can be observed, the amount of directional variation is greater for wavelengths associated with relatively low spectrometric reflectance values as reported by Hudson et al. (2006). This trend is also consistent with observations made by Xiong et al. (2015). For 1800 nm, they note that grain shape plays an important role in bidirectional reflectance modeling, and that models employing only spherical snow grains tend to overestimate the amount of scattering in the forward direction. For 600 nm, where the total reflectance is greater, the angular dependence is weaker. However, as indicated by Xiong et al. (2015), models employing non-spherical grains are able to reproduce the bidirectional reflectance pattern with greater fidelity. This effect of grain shape on directional reflectance aids in the characterization of snow surface scattering properties since snow tends to have a high reflectance in the forward direction when the angle of incidence is in the neighbourhood of 70° (Ding et al., 2019).

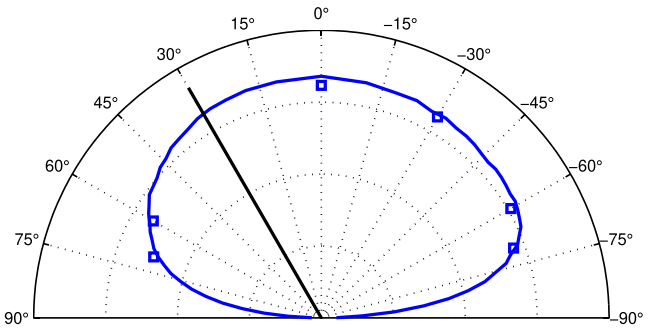

Fig. 15. Comparison of measured Dumont et al., 2010) data points and a simulated BRDF curve through the principal plane. A wavelength of 600 nm and an angle of incidence of 30° were employed to allow for qualitative comparisons between the simulated curve (blue solid line) and the data points (blue squares) provided by Dumont et al. (2010). The remaining sample characterization data are provided in Table 1. The angle of incidence for both measured and simulated data is indicated as a black solid line. (For interpretation of the references to colour in this figure legend, the reader is referred to the web version of this article.)

In addition to the behaviors highlighted above, Dumont et al. (2010) identified two other qualitative trends related to the polar angle of incidence. These trends can also be reproduced by the SPLITSnow model as described next.

The first trend refers to a nearly Lambertian behavior of snow reflectance for an angle of incidence of 0°. The blue solid curve in Fig. 19 indicates that the proposed model can capture this behavior.

The second trend noted by Dumont et al. (2010) is that at an incident angle of 30°, the forward scattering peak becomes apparent. Similarly, the SPLITSnow model can also capture this behavior as indicated by the red dashed curve in Fig. 19. Dumont et al. (2010) further remarked that, at 60° incident, the forward scattering peak is even more pronounced. This is also reproduced by our simulation as demonstrated by the green dotted curve in Fig. 19.

Besides the trends outlined above, Dumont et al. (2010) also noted that grain size has a measurable effect on directional reflectance. They observed that their maximum reflectance factor was higher for the samples that consisted of smaller grains. However, Warren et al. (1998) indicated that this phenomenon is wavelength dependent, *i.e.*, when absorption is high and grain sizes are large, the opposite is to be expected. To determine whether the proposed model can also account for these behaviors, we conducted *in silico* experiments in which we varied both the wavelength and the average grain size.

Fig. 20 presents the results of the experiment that reproduces the behavior reported by Dumont et al. (2010) outlined earlier. In this experiment, we considered a wavelength of 600 nm and an angle of incidence of 67°. At 600 nm the absorption coefficients for both water and ice are low (see Fig. 5). Note that the forward scattering peak with the smallest magnitude was elicited by the fine grained snow.

Fig. 21 presents the results of the experiment that reproduces the behavior reported by Warren et al. (1998). In this experiment, we considered a wavelength of 1450 nm. We note that the extinction coefficient values for water and ice at this wavelength are higher than those at 600 nm (Fig. 5). The angle of incidence and the grain sizes are the same as those used to generate the results presented in Fig. 20. As it can be verified in these results, the fine grained snow elicited the forward scattering peak with the greatest magnitude. Thus, the SPLITSnow model correctly predicts the wavelength dependency observed by Warren et al. (1998).

Finally, we performed an experiment to investigate the effect of facetness on directional reflectance. *In situ* controlled experiments assessing this effect are not readily documented in the literature. However, anecdotal evidence exists to suggest that facets should have an impact on directional reflectance (Dumont et al., 2010). Indeed, the results of our experiment, which are presented in Fig. 22, indicate that samples whose grains are characterized by low facetness (rounded shape) exhibit greater angular variation for their BRDF values than samples whose grains are characterized by high facetness (faceted shape).

5.4. Input-sensitivity analysis

The previous sections illustrated the effects of various input parameters on qualitative trends for both spectral and directional outputs. In this section, we present an input sensitivity analysis (Hamby, 1994, 1995) of those parameters.

To compute the mean sensitivity index (MSI) for reflectance, one parameter is selected to test, and two simulations are executed for that

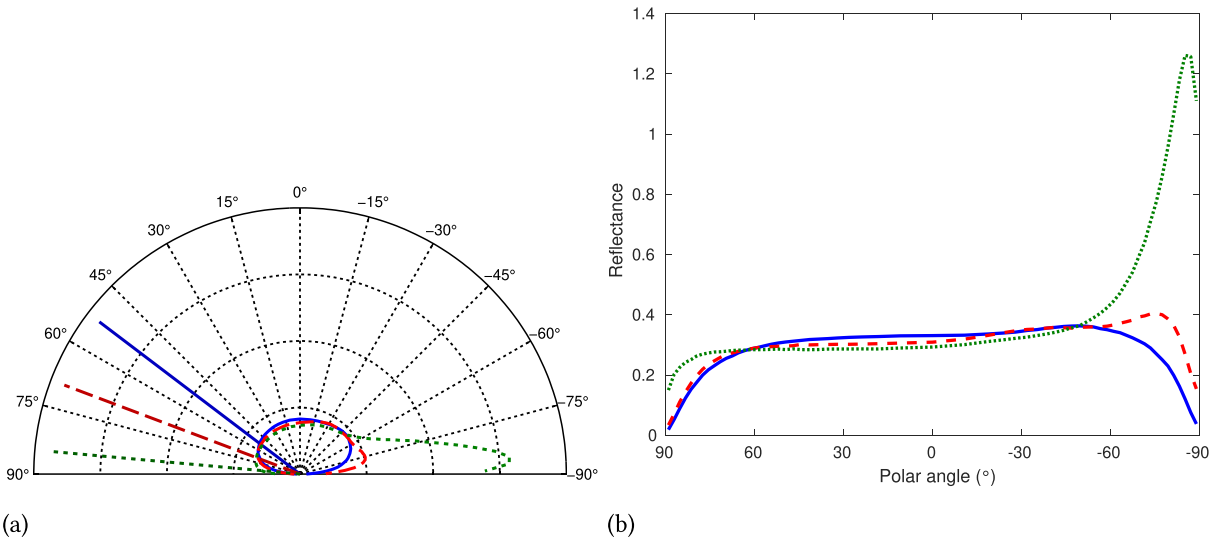

Fig. 16. BRDF plots (through the principal plane) computed for the selected sample. A wavelength of 600 nm and three angles of incidence, namely 52.8° (blue solid curve), 69.3° (red dashed curve), and 84.8° (green dotted curve) were employed to allow predictive comparisons with the results provided by Hudson et al. (2006). The snow depth is set to 25 cm. The remaining sample characterization parameter values are provided in Table 1. In (a), a polar plot is used to depict the profile, and the angles of incidence are indicated with matching lines. In (b), reflectance is plotted against the viewing polar angle, where positive polar angles are in the direction of incidence. (For interpretation of the references to colour in this figure legend, the reader is referred to the web version of this article.)

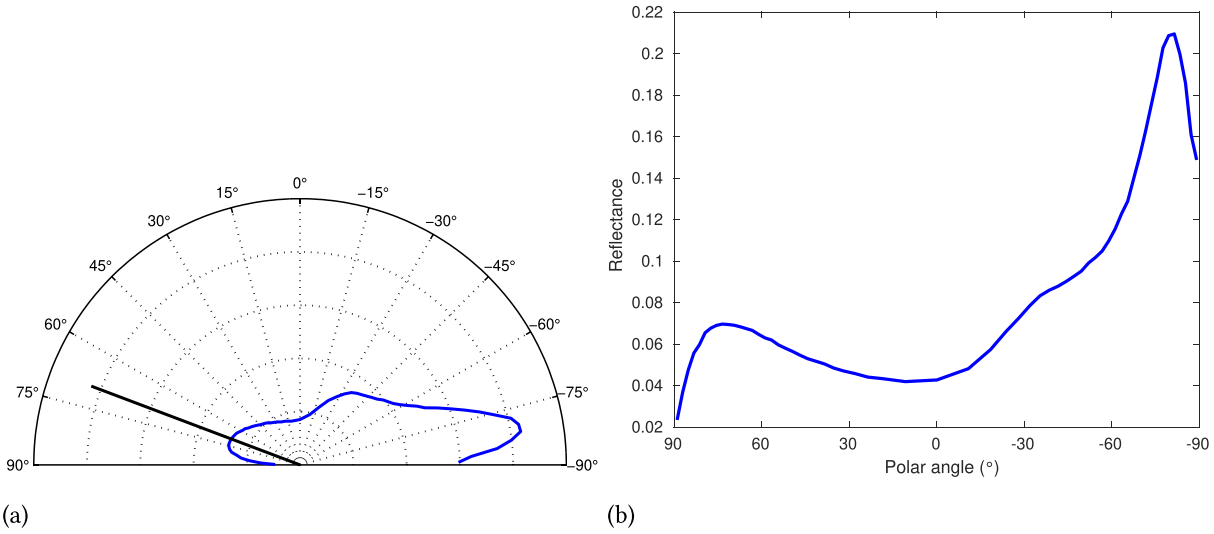

Fig. 17. BRDF plot (through the principal plane) computed for the selected sample. A wavelength of 1800 nm and the angle of incidence, namely 69.3°, were employed to allow qualitative comparisons with the data provided by Hudson et al. (2006). The snow depth is set to 25 cm. The remaining sample characterization parameter values are provided in Table 1. In (a), a polar plot is used to depict the profile, and the angle of incidence is indicated with a black solid line. In (b), reflectance is plotted against the viewing polar angle, where positive polar angles are in the direction of incidence.

parameter: one for the minimum parameter value; and one with the maximum parameter value. The MSI is computed using these two spectral outputs. All other baseline parameter values are set to the values presented in Table 1. Note that some input parameters are interval-based. For example, grain size is a uniform distribution between two grain size values. For these parameters, lower and upper bounds are selected so that they are close to the minimum and maximum values, while still providing a representative range. For grain size, an interval of 100–200 μm was selected for the minimum, which yields an average grain size of 150 μm. An interval of 900–1000 μm with an average grain size of 950 μm was selected for the maximum. For the facetness parameter, the minimum curve was produced using an interval of 0–0.2 and a mean of 0.1, while the maximum curve was produced using an interval of 0.8–1 with a mean of 0.9.

For each parameter, the MSI was computed using the following expression:

$$\mathrm{MSI} = \frac{1}{n}\sum_{i=1}^{n}\frac{\left|y_i - \widehat{y}_i\right|}{max\left\{y_i\widehat{y}_i\right\}}$$

where y_i is the baseline reflectance value, $\widehat{y}_i$ is the result after parameter variation, i is one of the sampled wavelengths, and n is the number of samples.

The transmittance MSI values were computed in a similar fashion to the reflectance MSI values, except that the sample depth parameter was set to 2 cm. This sample depth was used in order to be consistent with the results presented in Section 5.2.2. We remark that the sensitivity values for transmittance are dependent upon the selected depth. However, the

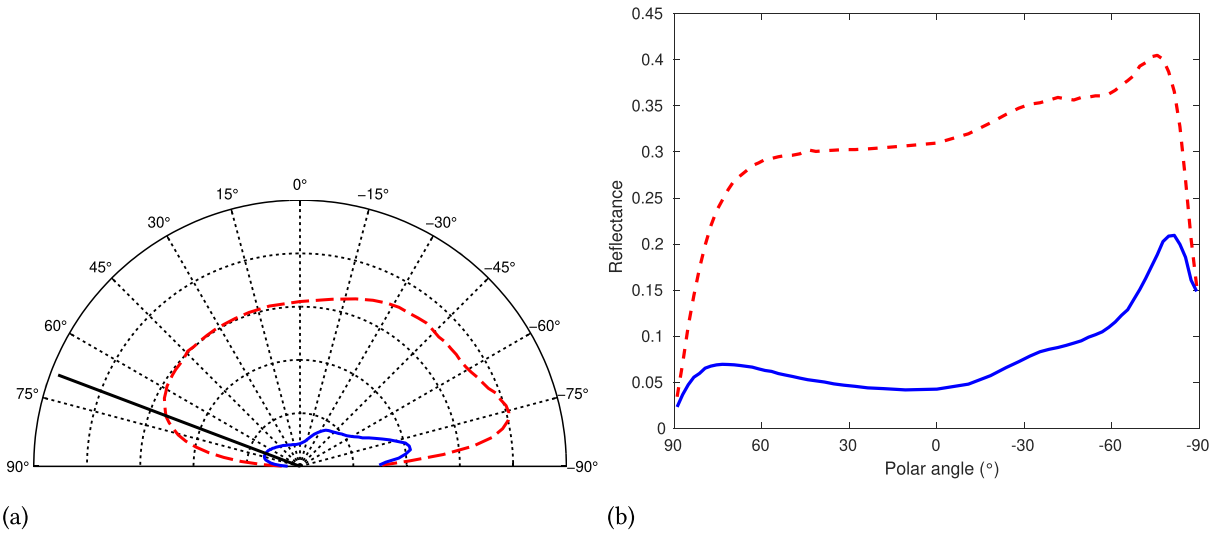

Fig. 18. BRDF plots (through the principal plane) computed for the selected sample. An incident angle of 69.3° and two wavelengths, namely 600 nm (red dashed curve), and 1800 nm (blue solid curve), were employed to allow qualitative comparisons with the data provided by Hudson et al. (2006). The snow depth is set to 25 cm. The remaining sample characterization parameter values are provided in Table 1. In (a), a polar plot is used to depict the profile, and the angle of incidence is indicated with a black solid line. In (b), reflectance is plotted against the viewing polar angle, where positive polar angles are in the direction of incidence. (For interpretation of the references to colour in this figure legend, the reader is referred to the web version of this article.)

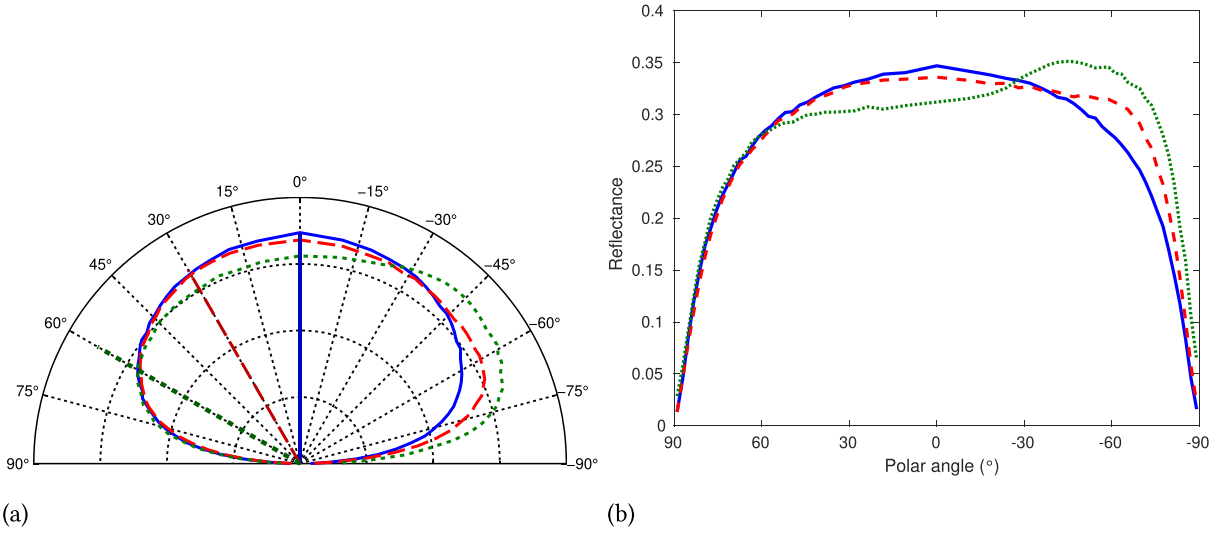

Fig. 19. BRDF plots (through the principal plane) computed for the selected sample. A wavelength of 600 nm and three angles of incidence, namely 0° (blue solid curve), 30° (red dashed curve), and 60° (green dotted curve) were employed to allow qualitative comparisons with the data provided by Dumont et al. (2010). The remaining sample characterization parameter values are provided in Table 1. In (a), a polar plot is used to depict the profile, and the angles of incidence are indicated with matching lines. In (b), reflectance is plotted against the viewing polar angle, where positive polar angles are in the direction of incidence. (For interpretation of the references to colour in this figure legend, the reader is referred to the web version of this article.)

relative input sensitivity in the neighbourhood of this depth is likely to be maintained.

Fig. 23 presents the MSI values produced by the sensitivity analysis for both reflectance and transmittance. The same values are reproduced numerically in Table 2. We remark that the effects of grain size on snow reflectance have been examined in several related works (Nolin and Dozier, 1993; Nakamura et al., 2001; Green et al., 2002; Jin et al., 2008; Lyapustin et al., 2009). The sensitivity of snow reflectance is also demonstrated by the MSI value for that parameter. We further remark that density is known to have little effect on snow reflectance (Bohren and Beschta, 1979). This is corroborated by the corresponding lowest MSI value obtained for that parameter.

As it can also be observed in Fig. 23 and Table 2, the MSI values for transmittance differ from those of reflectance. We remark that transmittance studies are more scarce than reflectance. However, one trend in particular is evident. More specifically, the sensitivity of snow transmittance to grain size is due to its impact on light scattering (Ciani et al., 2005). This trend accounts for the high MSI associated with grain size for transmittance.

5.5. Example application to remote observations

In this section, we provide an example application of the proposed model in the analysis of remote sensing data. Simulated curves are compared to data acquired from the Airborne Visible/Infrared Imaging Spectrometer Next Generation (AVIRIS-NG) instrument (Green et al., 1998; Hamlin et al., 2011).

We compared simulated values with values obtained from selected

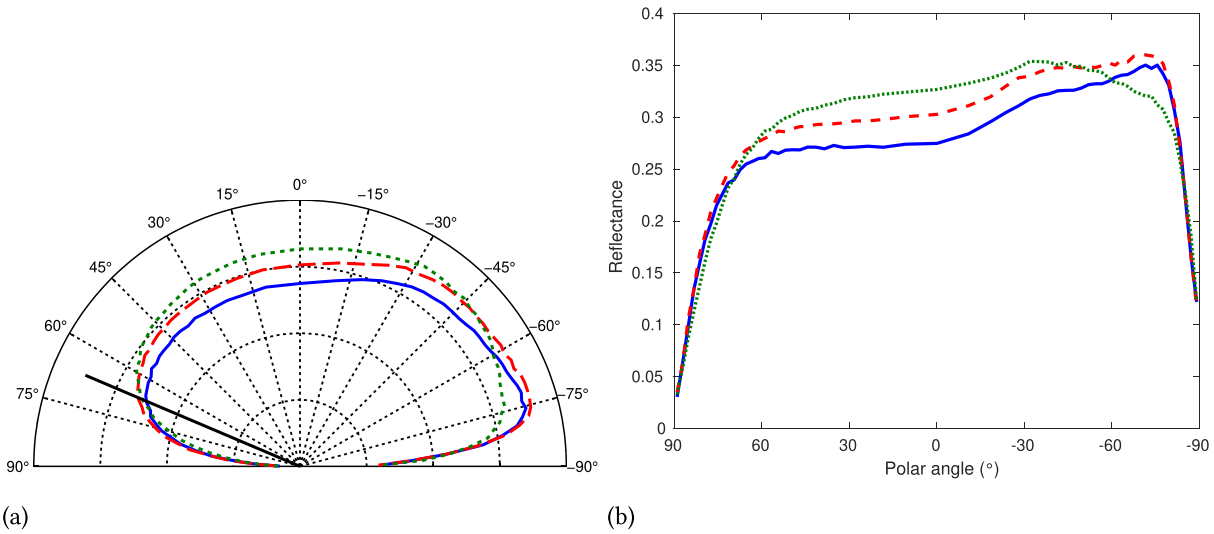

Fig. 20. BRDF plots (through the principal plane) computed for the selected sample. A wavelength of 600 nm and a (polar) angle of incidence of 67° were employed. The blue solid curve is associated with the presence of coarse-sized grains (1.5–3 mm), the red dashed curve with the presence of middle-sized grains (as specified in Table 1), and the green dotted curve with the presence of fine-sized grains (0.03–0.3 mm). The remaining sample characterization parameter values are provided in Table 1. In (a), a polar plot is used to depict the profile, and the angle of incidence is indicated with a black solid line. In (b), reflectance is plotted against the viewing polar angle, where positive polar angles are in the direction of incidence. (For interpretation of the references to colour in this figure legend, the reader is referred to the web version of this article.)

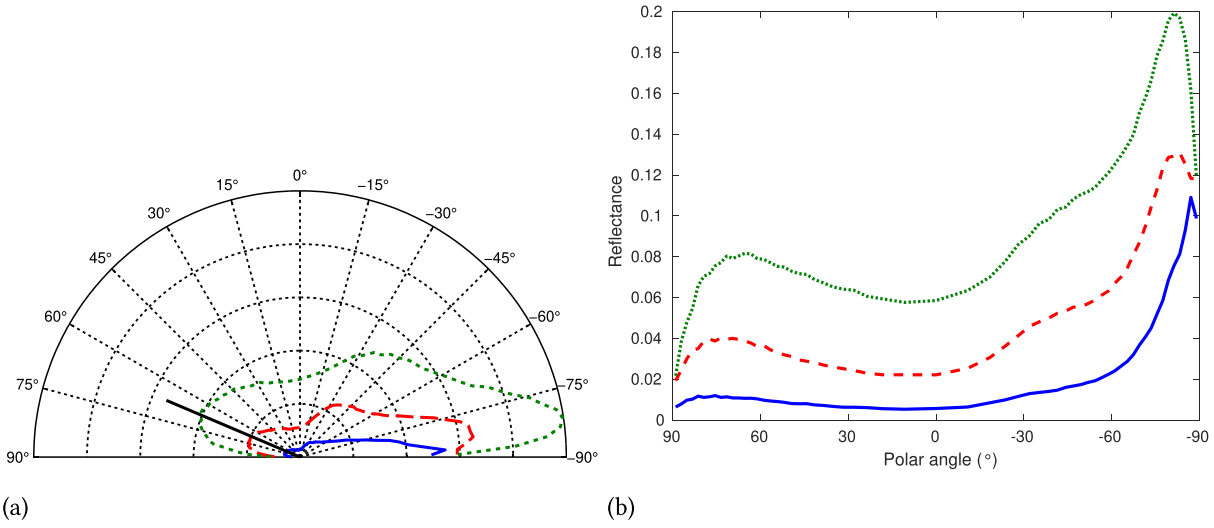

Fig. 21. BRDF plots (through the principal plane) computed for the selected sample. A wavelength of 1450 nm and a (polar) angle of incidence of 67° were employed. The blue solid curve is associated with the presence of coarse-sized grains (1.5–3 mm), the dashed red curve with the presence of middle-sized grains (as specified in Table 1), and the green dotted curve with the presence of fine-sized grains (0.03–0.3 mm). The remaining sample characterization parameter values are provided in Table 1. In (a), a polar plot is used to depict the profile, and the angle of incidence is indicated with a black solid line. In (b), reflectance is plotted against the viewing polar angle, where positive polar angles are in the direction of incidence. (For interpretation of the references to colour in this figure legend, the reader is referred to the web version of this article.)

pixels from flight line *ang20160217t074158*, which was captured over the mountainous state of Himachal Pradesh, India. This flight line was chosen due to the abundance of snow and since cloud conditions were listed as clear. The solar altitude at the time of the flight was 27.7°, or 62.3° away from the vertical.

Selecting a mountainous region introduces a challenge to the study of reflectance since the slope of the terrain affects the angle incidence of the light from the sun. To compensate for this, we used the estimated elevation data provided in the dataset to compute the gradient (which quantifies the rate of change of elevation) for each pixel. These gradients were then used to find a 5 × 5 area exhibiting little horizontal and vertical change in elevation. The selected pixels have a maximum gradient of 0.165 and a mean gradient of 0.067. Eight of the selected pixels have a gradient smaller than 0.1. The average reflectance was then computed for the 25 selected pixels.

Fig. 24 presents the results of this study. In Fig. 24(a), the selected area of study is displayed using a portion of the quicklook image dataset. The inset image is a 500% magnification of the region enclosed by the red square. No interpolation was used so that the original pixel values are preserved. The black square within the inset image demarcates the 25 pixels selected for analysis. In Fig. 24(b), a comparison between the average measured reflectance values of the selected region (black squares) with values produced using the SPLITSnow model (blue curve) is provided. Bars are used to indicate the minimum and maximum

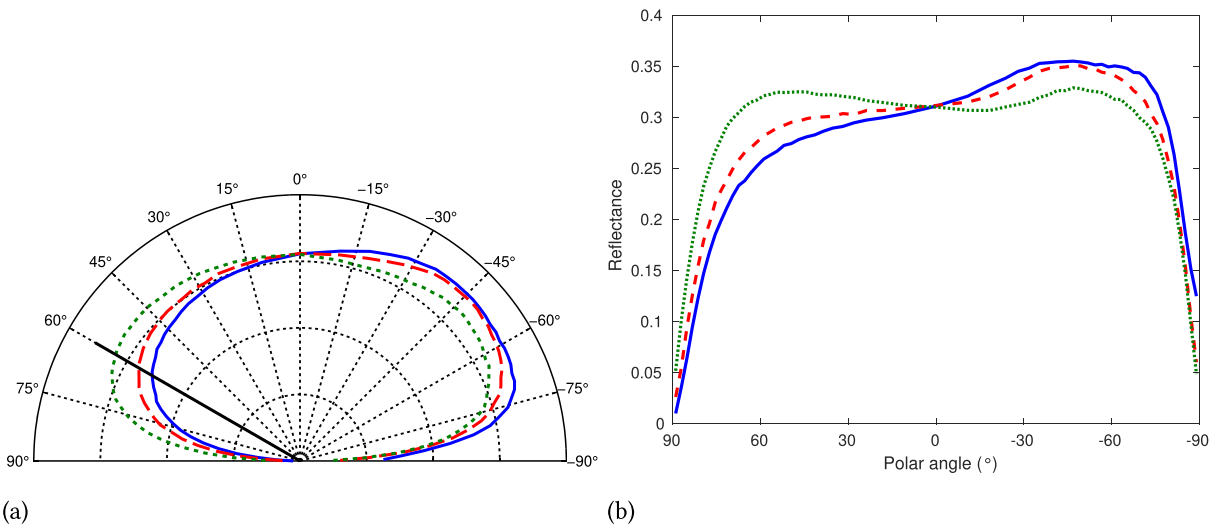

Fig. 22. BRDF plots (through the principal plane) computed for the selected sample. A wavelength of 600 nm and a (polar) angle of incidence of 60° were employed. The blue solid curve is associated with low facetness (0.0–0.2), the red dashed curve is associated with an intermediate facetness (0.2–0.4), and the green dotted curve is associated with a high facetness (0.8–1.0). The remaining sample characterization parameter values are provided in Table 1. In (a), a polar plot is used to depict the profile, and the angle of incidence is indicated with a black solid line. In (b), reflectance is plotted against the viewing polar angle, where positive polar angles are in the direction of incidence. (For interpretation of the references to colour in this figure legend, the reader is referred to the web version of this article.)

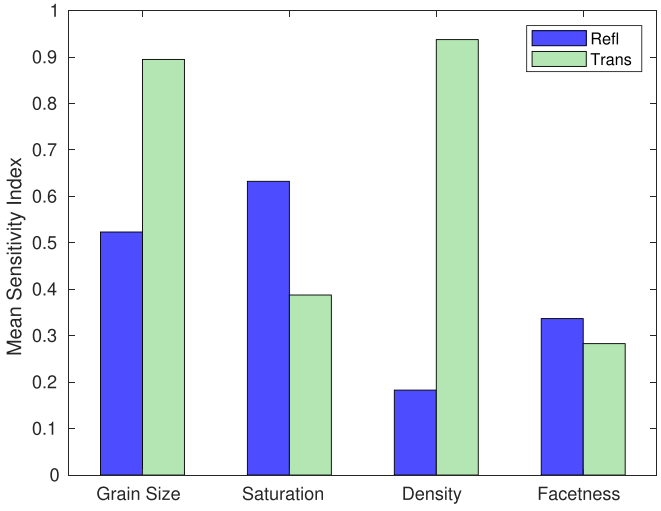

Fig. 23. Mean sensitivity index (MSI) values for the snow characterization parameters investigated in this work for both reflectance (Refl) and transmittance (Trans). The MSI calculations were carried out using spectral reflectance and transmittance curves computed considering the minimum and maximum values (from physically valid ranges) for each selected parameter, and maintaining the remaining parameters (depicted in Table 1 fixed. In the case of MSI values for transmittance, the snow depth was set to 2 cm.

Table 2
Mean sensitivity index (MSI) values for the snow characterization parameters investigated in this work. We note that the relative differences among these values are visually depicted in Fig. 23.

	Grain Size	Saturation	Density	Facetness
Reflectance	0.523	0.633	0.183	0.337
Transmittance	0.895	0.388	0.938	0.283

reflectance values for the 25 pixels.

We remark that interpretation of signals detected from instrumentation aboard aircraft is more difficult compared to field studies and laboratory experiments (Kokhanovsky, 2008), and compensation is

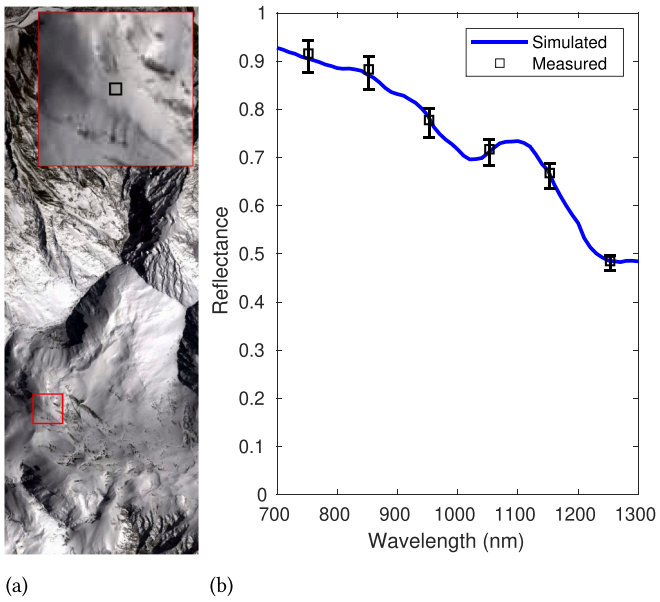

Fig. 24. Comparison of measured data provided by AVIRIS-NG Hamlin et al. (2011) and simulated data. The simulated directional-hemispherical reflectance curve was obtained using the SPLITSnow model and the sample characterization data provided in Table 1, except that the snow depth was set to 25 cm and the angle of incidence was set to 62.3°. A portion of the quicklook image from the *ang20160217t074158* flight line over Himachal Pradesh, India, is presented in (a). The inset image presents an enlargement of the region of study that has not been interpolated. The selected pixels are demarcated by a black square in the inset image. This region is represented by a grid of 5 × 5 pixels. In (b), the simulated reflectance curve is depicted by the blue solid line. The black squares indicate the average reflectance values for the 25 selected pixels and the bars indicate the minimum and maximum values for the selected pixels. (For interpretation of the references to colour in this figure legend, the reader is referred to the web version of this article.)

required for atmospheric absorption and scattering (Gao and Goetz, 1990; Thompson et al., 2015). Thus, the comparisons detailed in this section were performed against the "Level 2" algorithm correction

outputs that attempt to reduce measurement biases over snow-covered terrain (Thompson et al., 2015).

Gao and Goetz (1990) note that atmospheric water vapor transmittances are greater than 99% in narrow bands surrounding specific wavelengths, 840 nm, 1040 nm and 1240 nm, whereas other wavelength bands, such as 940 nm and 1140 nm, are sensitive to water vapor absorption. To minimize bias due to atmospheric water vapor, we provide a comparison between simulated and measured reflectance values for three wavelengths at which high transmission was observed. These data are presented in Table 3. The three wavelengths presented in the table were chosen among those employed by the AVIRIS-NG instrument directly since they are the nearest to the high-transmittance bands described by Gao and Goetz (1990). The simulated values were also computed using the same wavelengths for the purpose of direct comparison. The relative errors between average measured pixel values and the simulated values are all below 2.3%. The mean percent difference for the minimum and maximum values is 3.6%. Hence, the results of our comparisons indicate that the predictions provided by the proposed model can contribute to the reliable interpretation of remote sensing signals from snow-covered landscapes. Furthermore, they may also aid in the determination of aerosol optical thickness where advanced surface reflectance models are needed by elucidating the surface contribution to top-of-atmospheric reflectance (Kokhanovsky, 2008).

Table 3
Comparison of measured (obtained from the AVIRIS-NG dataset) and simulated reflectance values at selected wavelengths. The measured values correspond to the reflectances of the 25 pixels forming the region (inset) shown in Fig. 24(a), and the simulated values were computed using the proposed model.

Wavelength (nm)	Simulated	Measured		
		Mean	Minimum	Maximum
842.25	0.878	0.890	0.848	0.916
1073.76	0.692	0.701	0.669	0.721
1237.93	0.495	0.484	0.464	0.496

6. Conclusion and future work

In this work, we presented SPLITSnow, a novel first-principles light transport model for snow. Its predictive capabilities have been quantitatively and qualitatively evaluated through comparisons with measured data and phenomenological traits observed in field experiments described in the literature. The results of these comparisons indicate that the proposed model can be used to obtain high fidelity hyperspectral responses from snow samples with distinct characterizations.

The stochastic approach employed by the SPLITSnow model allows for efficient simulations of complex optical phenomena involving light interactions with large quantities of snow grains. Spheroids with non-trivial surface properties are used in the representation of the snow grains, which are generated on the fly as needed. This approach has a high fidelity-to-cost ratio, when compared with a traditional ray tracing approach that stores individual grains.

Dumont et al. (2010) reported that, although previous modeling efforts were able to accurately reproduce spectral albedo, the non-sphericity of natural snow grains limited the accurate modeling of snow BRDF. The SPLITSnow model is able to overcome these barriers. Furthermore, its formulation allows for the *in silico* study of individual parameters that are difficult or costly to take into account in field and lab experiments. For example, the ability to perform experiments on both rounded grains and faceted crystals serves to highlight the usefulness of the SPLITSnow model.

Predictive simulations of light interactions with snow grains have numerous applications in remote sensing and related fields. An understanding of how various snow grain characteristics affect reflectance and transmittance is necessary to identify and quantify properties of natural snowpack. As future work, we plan to extend the model's formulation to include pollutants so that their effect on snowpack reflectance and transmittance may be readily studied. The importance of this is evident since even a small amount of impurities may significantly reduce reflectance (Warren and Wiscombe, 1980), and direct comparisons could be made to artificial snow containing soot (Kokhanovsky, 2013). It is also our intention to apply the SPLITSnow model to examine snowpacks with different characterizations so that improved estimates of their morphological features can be obtained. This may require adding a layering system to the model's formulation so that different grain characterizations can be used at various depths of the snowpack.

In order to foster new advances in this area, the scientific community needs to provide continuing support for field studies aimed at the collection of hyperspectral datasets on snow radiometric responses to distinct illumination and environmental conditions. To increase their usefulness, these datasets should include detailed characterizations of the measured snow samples to facilitate accurate reproduction of the spectral responses through *in silico* experiments. We believe that the pairing of measurement efforts with *in silico* investigations will be instrumental to strengthen the knowledge foundation required for the development of more effective technologies aimed at the remote sensing of snow and snow-covered targets.

Declaration of competing interest

The authors declare that they have no known competing financial interests or personal relationships that could have appeared to influence the work reported in this paper.

Acknowledgements

This work was supported by the Natural Sciences and Engineering Research Council of Canada (NSERC-Discovery Grant 238337). The AVIRIS-NG data used in this study are available upon request at http://avirisng.jpl.nasa.gov/. The authors would like to thank the editorial staff and anonymous reviewers who invested considerable time and effort to improve this paper.

Appendix A. Average particle distance computation

In this appendix, we outline the main steps involved in the computation of the mean distance between grains, which is denoted by $\overline{d}$, and used in Eq. (1). We remark that this quantity is dependent upon the density of the targeted snow sample. Initially, we convert density to porosity, which is denoted by $\mathscr{P}$. Porosity is a unitless value that represents the volume fraction of a snow sample not occupied by its constituent grains. This is done using the method described by Kinar and Pomeroy (2015) using the following expression:

$$\mathscr{P} = 1 - \frac{D}{D_{ice}} \tag{A.1}$$

where D is the density of snow, and D_{ice} is the density of ice. The density of ice varies with temperature. This necessitates adding snow temperature, T,

as an input parameter to the model. From this, the density of ice is linearly interpolated using the data provided by Rumble (2019). Note that porosity is the complement to concentration, $\mathscr{C}$, which can accordingly be expressed as:

$$\mathscr{C} = 1 - \mathscr{P} \tag{A.2}$$

To compute the mean distance between snow grains, we employ the following equation (Kimmel and Baranoski, 2007):

$$\overline{d} = \frac{1}{\mathscr{C}K} \tag{A.3}$$

where K represents the cross-sectional area of snow grains per unit volume as seen in the direction of the ray. This quantity (which has units [m^{-1}]) is defined as:

$$K = \int_{\chi} n(x)G(x)\mathrm{d}x \tag{A.4}$$

where χ represents the set of all grain geometries, x is a member of that set, $n(x)$ represents the number probability density of picking a grain with geometry x, and $G(x)$ is the cross-sectional area of x projected onto the plane. The integral defining K is separable (Kimmel and Baranoski, 2007) into:

$$K = K_1 K_2 \tag{A.5}$$

where K_1 models the grain size distribution and K_2 accounts for shape. For uniformly distributed grain sizes, an analytic solution for K_1 can be obtained by simplifying the following definite integral:

$$K_1 = \frac{\int_{\mu_{min}}^{\mu_{max}} s^{-2}P(\mu)\mathrm{d}\mu}{\int_{\mu_{min}}^{\mu_{max}} s^{-1}P(\mu)\mathrm{d}\mu} \tag{A.6}$$

where $P(\mu) = 1/(\mu_{max} - \mu_{min})$ is the probability density function for a uniform distribution in the range of $[\mu_{min}, \mu_{max}]$. This simplifies to:

$$K_1 = \frac{\mu_{max} - \mu_{min}}{\mu_{min}\mu_{max}(ln(\mu_{min}) - ln(\mu_{max}))} \tag{A.7}$$

For normally distributed sphericity, K_2 reduces to:

$$K_2 = \frac{\int_{\Psi_{min}}^{\Psi_{max}} A(\Psi)\Phi\left(\overline{\Psi}, \sigma_{\Psi}^2\right)(\Psi)d\Psi}{4\int_{\Psi_{min}}^{\Psi_{max}} \Phi\left(\overline{\Psi}, \sigma_{\Psi}^2\right)(\Psi)d\Psi} \tag{A.8}$$

where $\Phi\left(\overline{x}, \sigma^2\right)(x)$ is the probability density function for a normally distributed random variable with mean $\overline{x}$ and standard deviation of σ, $A(\Psi)$ is the surface area to volume ratio of a prolate spheroid with $s = 2b = 1$ (where b is the semi-major axis), and Ψ represents inscribed circle sphericity (Kimmel and Baranoski, 2007). The quantity $A(\Psi)$ is given by:

$$A(\Psi) = 3\left(1 + \frac{sin^{-1}\sqrt{1-\Psi^4}}{\Psi^2\sqrt{1-\Psi^4}}\right) \tag{A.9}$$

The limits of integration for Eq. (A.8), Ψ_{min} and Ψ_{max}, are used to restrict the numeric solution to the specified range of grain sphericities. Accordingly, there are four model parameters that categorize the sphericity, namely Ψ_{min}, Ψ_{max}, σ_{Ψ}, and $\overline{\Psi}$.

Note that, even though it is numerically complex to calculate $\overline{d}$ given the density, this operation only needs to be performed once as a pre-computation at the beginning of a simulation. It can then be used to compute the distance to the next particle in the ray's path using Eq. (1).

References

Bänninger, D., Flühler, H., 2004. Modeling light scattering at soil surfaces. IEEE T. Geosci. Remote 42, 1462–1471. https://doi.org/10.1109/TGRS.2004.828190.

Bänninger, D., Bourgeois, C.S., Matzl, M., Schneebeli, M., 2008. Reflectance modeling for real snow structures using a beam tracing model. Sensors 8, 3482–3496. https://doi.org/10.3390/s8053482.

Baranoski, G.V.G., Rokne, J.G., Xu, G., 2001. Virtual spectrophotometric measurements for biologically and physically-based rendering. Vis. Comput. 17, 506–518. https://doi.org/10.1109/PCCGA.2000.883964.

Baranoski, G.V.G., Dimson, T., Chen, T.F., Kimmel, B., Yim, D., Miranda, E., 2012. Rapid dissemination of light transport models on the web. IEEE Comput. Graph. 32, 10–15. https://doi.org/10.1109/MCG.2012.58.

Barkstrom, B.R., 1972. Some effects of multiple scattering on the distribution of solar radiation in snow and ice. J. Glaciol. 11, 357–368. https://doi.org/10.1017/S0022143000022334.

Barnett, T.P., Adam, J.C., Lettenmaier, D.P., 2005. Potential impacts of a warming climate on water availability in snow-dominated regions. Nature 438, 303. https://doi.org/10.1038/nature04141.

Barry, R.G., 1985. The cryosphere and climate change. In: MacCracken, M.C., Luther, F. M. (Eds.), Detecting the Climatic Effects of Increasing Carbon Dioxide. US Dept. of Energy Washington, DC, Washington, DC. DOE/ER-0235. chapter 6, pp. 109–148.

Bartell, F., Dereniak, E., Wolfe, W., 1981. The theory and measurement of bidirectional reflectance distribution function (BRDF) and bidirectional transmittance distribution function (BTDF). In: Radiation Scattering in Optical Systems, International Society for Optics and Photonics, pp. 154–160. https://doi.org/10.1117/12.959611.

Beaglehole, D., Ramanathan, B., Rumberg, J., 1998. The UV to IR transmittance of Antarctic snow. J. Geoph. Res.-Atmos. 103, 8849–8857. https://doi.org/10.1029/97JD03604.

Bliss, D., Smith, H., 1985. Penetration of light into soil and its role in the control of seed germination. Plant Cell Environ. 8, 475–483. https://doi.org/10.1111/j.1365-3040.1985.tb01683.x.

Bohren, C.F., 1983. Colors of snow, frozen waterfalls, and icebergs. J. Opt. Soc. Am. 73, 1646–1652. https://doi.org/10.1364/JOSA.73.001646.

Bohren, C.F., Barkstrom, B.R., 1974. Theory of the optical properties of snow. J. Geophys. Res. 79, 4527–4535. https://doi.org/10.1029/JC079i030p04527.

Bohren, C.F., Beschta, R.L., 1979. Snowpack albedo and snow density. Cold Reg. Sci. Technol. 1, 47–50. https://doi.org/10.1016/0165-232X(79)90018-1.

Bohren, C.F., Huffman, D.R., 1983. Absorption and Scattering of Light by Small Particles. John Wiley & Sons, Toronto, Canada.

Born, M., Wolf, E., 1999. Principles of Optics: Electromagnetic Theory of Propagation, Interference and Diffraction of Light, 7 ed. Cambridge University Press, Cambridge, UK.

Ciani, A., Goss, K., Schwarzenbach, R., 2005. Light penetration in soil and particulate materials. Eur. J. Soil Sci. 56, 561–574. https://doi.org/10.1111/j.1365-2389.2005.00688.x.
Colbeck, S.C., 1982. An overview of seasonal snow metamorphism. Rev. Geophys. 20, 45–61. https://doi.org/10.1029/RG020i001p00045.
Colbeck, S.C., 1997. A Review of Sintering in Seasonal Snow. Technical Report 97-10. U. S. Army Cold Regions Research and Engineering Lab. Hanover, NH, USA. https://doi.org/10.21236/ADA335556.
Cook, R.L., Torrance, K.E., 1982. A reflectance model for computer graphics. ACM T. Graphic. 1, 7–24. https://doi.org/10.1145/800224.806819.
Ding, A., Jiao, Z., Dong, Y., Zhang, X., Peltoniemi, J.I., Mei, L., Guo, J., Yin, S., Cui, L., Chang, Y., Xie, R., 2019. Evaluation of the snow albedo retrieved from the snow kernel improved the Ross-Roujean BRDF model. Remote Sens. 11, 1611. https://doi.org/10.3390/rs11131611.
Dozier, J., Painter, T.H., 2004. Multispectral and hyperspectral remote sensing of Alpine snow properties. Annu. Rev. Earth Pl. Sc. 32, 465–494. https://doi.org/10.1146/annurev.earth.32.101802.120404.
Dumont, M., Brissaud, O., Picard, G., Schmitt, B., Gallet, J.C., Arnaud, Y., 2010. High-accuracy measurements of snow bidirectional reflectance distribution function at visible and NIR wavelengths – comparison with modelling results. Atmos. Chem. Phys. 10, 2507–2520. https://doi.org/10.5194/acp-10-2507-2010.
Dunkle, R.V., Bevans, J.T., 1956. An approximate analysis of the solar reflectance and transmittance of a snow cover. J. Meteorol. 13, 212–216. https://doi.org/10.1175/1520-0469(1956)013.
Fierz, C., Armstrong, R.L., Durand, Y., Etchevers, P., Greene, E., McClung, D.M., Nishimura, K., Satyawali, P.K., Sokratov, S., 2009. The international classification for seasonal snow on the ground. In: Technical Report 83. Paris, France, UNESCO-IHP.
Gao, B.C., Goetz, A.F.H., 1990. Column atmospheric water vapor and vegetation liquid water retrievals from airborne imaging spectrometer data. J. Geoph. Res.-Atmos. 95, 3549–3564. https://doi.org/10.1029/JD095iD04p03549.
Gedney, S.D., 2011. Introduction to the Finite-Difference Time-Domain (FDTD) Method for Electromagnetics. volume 27 of Synthesis Digital Library of Engineering and Computer Science. Morgan & Claypool, San Rafael, CA, USA. https://doi.org/10.2200/S00316ED1V01Y201012CEM027.
Gergely, M., Schneebeli, M., Roth, K., 2010. First experiments to determine snow density from diffuse near-infrared transmittance. Cold Reg. Sci. Technol. 64, 81–86. https://doi.org/10.1016/j.coldregions.2010.06.005.
Gerland, S., Liston, G.E., Winther, J.G., Ørbæk, J.B., Ivanov, B.V., 2000. Attenuation of solar radiation in Arctic snow: field observations and modelling. Ann. Glaciol. 31, 364–368. https://doi.org/10.3189/172756400781820444.
Giddings, J.C., LaChapelle, E., 1961. Diffusion theory applied to radiant energy distribution and albedo of snow. J. Geophys. Res. 66, 181–189. https://doi.org/10.1029/JZ066i001p00181.
Green, R.O., Eastwood, M.L., Sarture, C.M., Chrien, T.G., Aronsson, M., Chippendale, B. J., Faust, J.A., Pavri, B.E., Chovit, C.J., Solis, M., Olah, M.R., Williams, O., 1998. Imaging spectroscopy and the airborne visible/infrared imaging spectrometer (AVIRIS). Remote Sens. Environ. 65, 227–248. https://doi.org/10.1016/S0034-4257(98)00064-9.
Green, R.O., Dozier, J., Roberts, D., Painter, T., 2002. Spectral snow-reflectance models for grain-size and liquid-water fraction in melting snow for the solar-reflected spectrum. Ann. Glaciol. 34, 71–73. https://doi.org/10.3189/172756402781817987.
Grenfell, T.C., Warren, S.G., 1999. Representation of a nonspherical ice particle by a collection of independent spheres for scattering and absorption of radiation. J. Geoph. Res.-Atmos. 104, 31697–31709. https://doi.org/10.1029/1999JD900496.
Gross, D., 1999. Report from the Fidelity Implementation Study Group, in: Spring Simulation Interoperability Workshop.
Grundy, W.M., Douté, S., Schmitt, B., 2000. A Monte Carlo ray-tracing model for scattering and polarization by large particles with complex shapes. J. Geoph. Res.-Planet. 105, 29291–29314. https://doi.org/10.1029/2000JE001276.
Hale, G.M., Querry, M.R., 1973. Optical constants of water in the 200-nm to 200-wavelength region. Appl. Opt. 12, 555–563. https://doi.org/10.1364/AO.12.000555.
Hall, D.K., Riggs, G.A., 2007. Accuracy assessment of the MODIS snow products. Hydrol. Process. 21, 1534–1547. https://doi.org/10.1002/hyp.6715.
Hamby, D., 1994. A review of techniques for parameter sensitivity analysis of environmental models. Environ. Monit. Assess. 32, 135–154. https://doi.org/10.1007/BF00547132.
Hamby, D., 1995. A comparison of sensitivity analysis techniques. Health Phys. 68, 195–204. https://doi.org/10.1097/00004032-199502000-00005.
Hamlin, L., Green, R., Mouroulis, P., Eastwood, M., Wilson, D., Dudik, M., Paine, C., 2011. Imaging spectrometer science measurements for terrestrial ecology: Aviris and new developments. In: Aerosp. Conf. Proc. IEEE, pp. 1–7. https://doi.org/10.1109/AERO.2011.5747395.
Hammersley, J.M., Handscomb, D.C., 1964. Monte Carlo Methods. Chapman and Hall, London, UK. URL. https://doi.org/10.1007/978-94-009-5819-7.
Han, P., Long, D., Han, Z., Du, M., Dai, L., Hao, X., 2019. Improved understanding of snowmelt runoff from the headwaters of China's Yangtze River using remotely sensed snow products and hydrological modeling. Remote Sens. Environ. 224, 44–59. https://doi.org/10.1016/j.rse.2019.01.041.
Haussener, S., Gergely, M., Schneebeli, M., Steinfeld, A., 2012. Determination of the macroscopic optical properties of snow based on exact morphology and direct pore-level heat transfer modeling. J. Geoph. Res.-Earth 117. https://doi.org/10.1029/2012JF002332.
Hudson, S.R., Warren, S.G., Brandt, R.E., Grenfell, T.C., Six, D., 2006. Spectral bidirectional reflectance of Antarctic snow: measurements and parameterization. J. Geoph. Res.-Atmos. 111 https://doi.org/10.1029/2006JD007290.
Jacquemoud, S., Ustin, S., Verdebout, J., Schmuck, G., Andreoli, G., Hosgood, B., 1996. Estimating leaf biochemistry using PROSPECT leaf optical properties model. Remote Sens. Environ. 56, 194–202. https://doi.org/10.1016/0034-4257(95)00238-3.
Jiao, Z., Ding, A., Kokhanovsky, A., Schaaf, C., Bréon, F.M., Dong, Y., Wang, Z., Liu, Y., Zhang, X., Yin, S., Cui, L., Mei, L., Chang, Y., 2019. Development of a snow kernel to better model the anisotropic reflectance of pure snow in a kernel-driven BRDF model framework. Remote Sens. Environ. 221, 198–209. https://doi.org/10.1016/j.rse.2018.11.001.
Jin, Z., Charlock, T.P., Yang, P., Xie, Y., Miller, W., 2008. Snow optical properties for different particle shapes with application to snow grain size retrieval and MODIS/CERES radiance comparison over Antarctica. Remote Sens. Environ. 112, 3563–3581. https://doi.org/10.1016/j.rse.2008.04.011.
Joseph, J.H., Wiscombe, W.J., Weinman, J.A., 1976. The delta-Eddington approximation for radiative flux transfer. J. Atmos. Sci. 33, 2452–2459. https://doi.org/10.1175/1520-0469(1976)033<2452:TDEAFR>2.0.CO;2.
Kaempfer, T.U., Hopkins, M.A., Perovich, D.K., 2007. A three-dimensional microstructure-based photon-tracking model of radiative transfer in snow. J. Geoph. Res.-Atmos. 112 https://doi.org/10.1029/2006JD008239.
Kim, R.S., Durand, M., Li, D., Baldo, E., Margulis, S.A., Dumont, M., Morin, S., 2019. Estimating alpine snow depth by combining multifrequency passive radiance observations with ensemble snowpack modeling. Remote Sens. Environ. 226, 1–15. https://doi.org/10.1016/j.rse.2019.03.016.
Kimmel, B.W., Baranoski, G.V.G., 2007. A novel approach for simulating light interaction with particulate materials: application to the modeling of sand spectral properties. Opt. Express 15, 9755–9777. https://doi.org/10.1364/OE.15.009755.
Kinar, N.J., Pomeroy, J.W., 2015. Measurement of the physical properties of the snowpack. Rev. Geophys. 53, 481–544. https://doi.org/10.1002/2015RG000481.
Knap, W.H., Reijmer, C.H., 1998. Anisotropy of the reflected radiation field over melting glacier ice: measurements in Landsat TM bands 2 and 4. Remote Sens. Environ. 65, 93–104. https://doi.org/10.1016/S0034-4257(98)00015-7.
Kokhanovsky, A.A., 2008. Aerosol Optics: Light Absorption and Scattering by Particles in the Atmosphere. Springer Science & Business Media, New York, NY, USA.
Kokhanovsky, A., 2013. Spectral reflectance of solar light from dirty snow: a simple theoretical model and its validation. Cryosphere 7, 1325–1331. https://doi.org/10.5194/tc-7-1325-2013.
Kokhanovsky, A.A., Zege, E.P., 2004. Scattering optics of snow. Appl. Opt. 43, 1589–1602. https://doi.org/10.1364/AO.43.001589.
Kokhanovsky, A., Smirnov, A., Korkin, S., Wind, G., Slutsker, I., 2020. The retrieval of cloud properties based on spectral solar light diffuse transmittance measurements under optically thick cloud cover conditions. J. Quant. Spectrosc. Ra 107008. https://doi.org/10.1016/j.jqsrt.2020.107008.
Krishnaswamy, A., Baranoski, G.V.G., Rokne, J.G., 2004. Improving the reliability/cost ratio of goniophotometric comparisons. J. Graph. Tools 9, 1–20. https://doi.org/10.1080/10867651.2004.10504894.
Lyapustin, A., Tedesco, M., Wang, Y., Aoki, T., Hori, M., Kokhanovsky, A., 2009. Retrieval of snow grain size over Greenland from MODIS. Remote Sens. Environ. 113, 1976–1987. https://doi.org/10.1016/j.rse.2009.05.008.
Metsämäki, S., Böttcher, K., Pulliainen, J., Luojus, K., Cohen, J., Takala, M., Mattila, O.P., Schwaizer, G., Derksen, C., Koponen, S., 2018. The accuracy of snow melt-off day derived from optical and microwave radiometer data–a study for Europe. Remote Sens. Environ. 211, 1–12. https://doi.org/10.1016/j.rse.2018.03.029.
Middleton, W.E.K., Mungall, A.G., 1952. The luminous directional reflectance of snow. J. Opt. Soc. Am. 42, 572–579. https://doi.org/10.1364/JOSA.42.000572.
Mishchenko, M.I., Dlugach, J.M., Yanovitskij, E.G., Zakharova, N.T., 1999. Bidirectional reflectance of flat, optically thick particulate layers: an efficient radiative transfer solution and applications to snow and soil surfaces. J. Quant. Spectrosc. Ra. 63, 409–432. https://doi.org/10.1016/S0022-4073(99)00028-X.
Nakamura, T., Abe, O., Hasegawa, T., Tamura, R., Ohta, T., 2001. Spectral reflectance of snow with a known grain-size distribution in successive metamorphism. Cold Reg. Sci. Technol. 32, 13–26. https://doi.org/10.1016/S0165-232X(01)00019-2.
Natural Phenomena Simulation Group, 2020a. Run SPLITSnow Online (Goniometric Mode). http://www.npsg.uwaterloo.ca/models/splitsnow-gonio.php.
Natural Phenomena Simulation Group, 2020b. Run SPLITSnow Online (Spectrometric Mode). http://www.npsg.uwaterloo.ca/models/splitsnow.php.
Needham, J., Lu, G.D., 1961. The earliest snow crystal observations. Weather 16, 319–327. https://doi.org/10.1002/j.1477-8696.1961.tb02589.x.
Nicodemus, F., Richmond, J., Hsia, J., Ginsberg, I., Limperis, T., 1977. Geometrical Considerations and Nomenclature for Reflectance. US Department of Commerce, National Bureau of Standards, Washinton, D.C, USA. URL. https://doi.org/10.6028/NBS.MONO.160.
Nolin, A.W., Dozier, J., 1993. Estimating snow grain size using AVIRIS data. Remote Sens. Environ. 44, 231–238. https://doi.org/10.1016/0034-4257(93)90018-S.
Nolin, A.W., Dozier, J., 2000. A hyperspectral method for remotely sensing the grain size of snow. Remote Sens. Environ. 74, 207–216. https://doi.org/10.1016/S0034-4257(00)00111-5.
Ollerhead, J., 2001. Light transmittance through dry, sieve sand: some test results. Ancient TL 19, 13–17.
Palmer, K.F., Williams, D., 1974. Optical properties of water in the near infrared. J. Opt. Soc. Am. 64, 1107–1110. https://doi.org/10.1364/JOSA.64.001107.
Pedrotti, F.L., Pedrotti, L.S., 1993. Introduction to Optics, Second ed. Prentice Hall, Upper Saddle River, NJ, USA.
Perovich, D.K., 2007. Light reflection and transmission by a temperate snow cover. J. Glaciol. 53, 201–210. https://doi.org/10.3189/172756507782202919.

Picard, G., Arnaud, L., Domine, F., Fily, M., 2009. Determining snow specific surface area from near-infrared reflectance measurements: numerical study of the influence of grain shape. Cold Reg. Sci. Technol. 56, 10–17. https://doi.org/10.1016/j.coldregions.2008.10.001.

Picard, G., Sandells, M., Löwe, H., 2018. SMRT: an active–passive microwave radiative transfer model for snow with multiple microstructure and scattering formulations (v1.0). Geosci. Model Dev. 11, 2763–2788. https://doi.org/10.5194/gmd-11-2763-2018.

Pope, R.M., Fry, E.S., 1997. Absorption spectrum (380–700 nm) of pure water. II. Integrating cavity measurements. Appl. Opt. 36, 8710–8723. https://doi.org/10.1364/AO.36.008710.

Riley, N.A., 1941. Projection sphericity. J. Sediment. Res. 11, 94–95. https://doi.org/10.1306/D426910C-2B26-11D7-8648000102C1865D.

Rumble, J.R., 2019. CRC Handbook of Chemisty and Physics, 100 ed. CRC Press/Taylor & Francis, Boca Raton, FL, USA (Internet Version).

Stamnes, K., Tsay, S.C., Wiscombe, W., Jayaweera, K., 1988. Numerically stable algorithm for discrete-ordinate-method radiative transfer in multiple scattering and emitting layered media. Appl. Opt. 27, 2502–2509. https://doi.org/10.1364/AO.27.002502.

Tester, M., Morris, C., 1987. The penetration of light through soil. Plant Cell Environ. 10, 281. https://doi.org/10.1111/j.1365-3040.1987.tb01607.x.

Thompson, D.R., Gao, B.C., Green, R.O., Roberts, D.A., Dennison, P.E., Lundeen, S.R., 2015. Atmospheric correction for global mapping spectroscopy: ATREM advances for the HyspIRI preparatory campaign. Remote Sens. Environ. 167, 64–77. https://doi.org/10.1016/j.rse.2015.02.010.

Tian, J., Philpot, W.D., 2018. Spectral transmittance of a translucent sand sample with directional illumination. IEEE T. Geosci. Remote 56, 4307–4317. https://doi.org/10.1109/TGRS.2018.2810815.

Torrance, K.E., Sparrow, E.M., 1967. Theory for off-specular reflection from roughened surfaces. J. Opt. Soc. Am. 57, 1105–1114. https://doi.org/10.1364/JOSA.57.001105.

Vepraskas, M., Cassel, D., 1987. Sphericity and roundness of sand in coastal plain soils and relationships with soil physical properties 1. Soil Sci. Soc. Am. J. 51, 1108–1112. https://doi.org/10.2136/sssaj1987.03615995005100050003x.

Wagner, W., Cooper, J., Dittmann, A., Kijima, J., Kretzschmar, H.J., Kruse, A., Mareš, R., Oguchi, K., Sato, H., Stöcker, I., Šifner, O., Takaishi, Y., Tanishita, I., Trübenbach, J., Willkommen, T., 2000. The IAPWS industrial formulation 1997 for the thermodynamic properties of water and steam. J. Eng. Gas Turbines Power 122, 150–184. https://doi.org/10.1115/1.483186.

Wang, B., Su, D., Liu, J., 2005. Analysis of snow covered radome with ray tracing method. In: APMC 2005. IEEE, pp. 1–3. https://doi.org/10.1109/APMC.2005.1606538.

Warren, S.G., 1984. Optical constants of ice from the ultraviolet to the microwave. Appl. Opt. 23, 1206–1225. https://doi.org/10.1364/AO.23.001206.

Warren, S.G., Brandt, R.E., 2008. Optical constants of ice from the ultraviolet to the microwave: a revised compilation. J. Geoph. Res.-Atmos. 113, D14220. https://doi.org/10.1029/2007JD009744.

Warren, S.G., Wiscombe, W.J., 1980. A model for the spectral albedo of snow. II: snow containing atmospheric aerosols. J. Atmos. Sci. 37, 2734–2745. https://doi.org/10.1175/1520-0469(1980)037<2734:AMFTSA>2.0.CO;2.

Warren, S.G., Brandt, R.E., Hinton, P.O., 1998. Effect of surface roughness on bidirectional reflectance of Antarctic snow. J. Geoph. Res.-Planet. 103, 25789–25807. https://doi.org/10.1029/98JE01898.

Wasserman, L., 2004. All of Statistics: A Concise Course in Statistical Inference. Springer, New York, NY, USA.

Wiscombe, W.J., Warren, S.G., 1980. A model for the spectral albedo of snow. I: pure snow. J. Atmos. Sci. 37, 2712–2733. https://doi.org/10.1175/1520-0469(1980)037<2712:AMFTSA>2.0.CO;2.

Woolley, J., Stoller, E., 1978. Light penetration and light-induced seed germination in soil. Plant Physiol. 61, 597–600. https://doi.org/10.1104/pp.61.4.597.

Xiong, C., Shi, J., 2014. Simulating polarized light scattering in terrestrial snow based on bicontinuous random medium and Monte Carlo ray tracing. J. Quant. Spectrosc. Ra. 133, 177–189. https://doi.org/10.1016/j.jqsrt.2013.07.026.

Xiong, C., Shi, J., 2017. A new snow light scattering model and its application in snow parameter retrieval from satellite remote sensing. In: Geoscience and Remote Sensing Symposium (IGARSS). IEEE, pp. 1473–1476. https://doi.org/10.1109/IGARSS.2017.8127245.

Xiong, C., Shi, J., 2018. Snow specific surface area remote sensing retrieval using a microstructure based reflectance model. Remote Sens. Environ. 204, 838–849. https://doi.org/10.1016/j.rse.2017.09.017.

Xiong, C., Shi, J., Ji, D., Wang, T., Xu, Y., Zhao, T., 2015. A new hybrid snow light scattering model based on geometric optics theory and vector radiative transfer theory. IEEE T. Geosci. Remote 53, 4862–4875. https://doi.org/10.1109/TGRS.2015.2411592.

Yang, P., Liou, K.N., 1996. Geometric-optics-integral-equation method for light scattering by nonspherical ice crystals. Appl. Opt. 35, 6568–6584. https://doi.org/10.1364/AO.35.006568.

Zhou, X., Li, S., Stamnes, K., 2003. Effects of vertical inhomogeneity on snow spectral albedo and its implication for optical remote sensing of snow. J. Geoph. Res.-Atmos. 108, 4738. https://doi.org/10.1029/2003JD003859.